Doctoral Dissertation

Studies on Novel Environmentally Friendly Yellow, Red, and Blue Inorganic Pigments

（新規な環境調和型の黄色、赤色、青色無機顔料に関する研究）

Wendusu

January 2015

Department of Applied Chemistry
Graduate School of Engineering
Osaka University

Studies on Novel Environmentally Friendly Yellow, Red, and Blue Inorganic Pigments

（新規な環境調和型の黄色、赤色、青色無機顔料に関する研究）

2015

Wendusu

Department of Applied Chemistry
Graduate School of Engineering
Osaka University

Preface

The work of this thesis has been carried out under the supervision of Professor Dr. Nobuhito Imanaka at Department of Applied Chemistry, Graduate School of Engineering, Osaka University.

The object of this thesis is to develop novel inorganic yellow, red, and blue pigments with high color performance.

The author wishes that the findings and the knowledge obtained in this work provide useful suggestions and information for further development and design of novel environmentally friendly inorganic pigments and that the materials would contribute to more practical applications.

Wendusu

Wendusu

Department of Applied Chemistry

Graduate School of Engineering

Osaka University

2-1 Yamadaoka, Suita,

Osaka 565-0871,

Japan

January 2015

Contents

Chapter 3

Synthesis of Novel Inorganic Blue Pigments Based on Calcium Scandium Silicate Garnet ($Ca_3Sc_2Si_3O_{12}$)

General Introduction

Pigments are colored fine powders that are insoluble or poorly-soluble in water and organic solvents. They are firmly fixed on or well dispersed in an object to be colored by the action of the dispersing media. The color of such pigment is determined by selective absorption of the visible light and the complementary color of the absorbed one is observable.

Generally, pigments fall into the general classification of organic and inorganic. Usually, organic pigments are brilliantly colored with a wide variety of hues and have relatively high tinting strength compared with those of inorganic ones. However, organic pigments have some limitations for practical uses due to low thermal stability and poor ultraviolet light resistance. In contrast, inorganic pigments based on oxides, nitrides, and sulfides have higher thermal stability and weather fastness than organic pigments.

On the other hand, inorganic pigments are applied in a wide range of products such as paints, inks, plastics, rubbers, ceramics, enamels, and glasses [1, 2]. Although there are various colors in inorganic pigments, the demands for pigments with three primary colors, *i.e.*, yellow, red, and blue, are exceptionally large after black and white pigments. For decades, several inorganic pigments, such as chrome yellow ($PbCrO_4$), cadmium zinc yellow (CdS-ZnS), titanate yellow (TiO_2-NiO-Sb_2O_3), red lead (Pb_3O_4 or 2PbO-PbO_2), cadmium selenide red (CdSe-CdS), mercuric sulfide red (HgS), and cobalt aluminate blue ($CoAl_2O_4$), have been used for many applications, because these compounds can exhibit brilliant colors. However, the use of these materials has been restricted because they contain toxic elements (Pb, Cr, Cd, Sb, Se, Hg, and Co), which are harmful not only to the human body but also to the environment.

Because of this situation, several nontoxic materials such as praseodymium yellow

($ZrSiO_4$: Pr), red iron oxide (Fe_2O_3), iron hexacyanoferrate ($Fe(III)_4[Fe(II)(CN)_6]_3$, Prussian blue), and sulfur-containing sodium aluminosilicate ($Na_{6-8}Al_6Si_6O_{24}S_{2-4}$, Ultramarine) have been employed as environmentally friendly inorganic pigments, but, unfortunately, their color performances are insufficient in comparison with those of the conventional toxic ones. Furthermore, iron hexacyanoferrate and sulfur-containing sodium aluminosilicate have poor chemical resistance to acidic and alkaline environments. In addition, the former has an explosion hazard; the ignition point is 600 − 625 ºC [2]. Although bismuth vanadate ($BiVO_4$) is a relatively new class of environmentally friendly inorganic yellow pigments and has gained steadily in importance over the last two decades [1], its tinting power is not enough as compared to those of the conventional toxic ones.

Although most of the existing inorganic pigments are oxide compounds, some rare earth sulfides, and oxynitrides, such as Ce_2S_3, La_2S_3, $Ce_4Si_3S_{12}$ [3, 4], $Ca_{(1-x)}La_xTaO_{(2-x)}N_{(1+x)}$, and $Sm_{14}W_4O_{33-3x}N_{2x}$ [5, 6], have been reported as possible nontoxic pigments because these compounds show various brilliant colors. Unfortunately, sulfides sometimes cause color changes when they are mixed with other pigments due to their poor chemical stability. In the case of the oxynitride compounds, toxic and flammable ammonia gas is required for their synthesis [5, 6]. Furthermore, both sulfide and oxynitride compounds involve a risk to generate toxic sulfur oxides (SO_x) and nitrogen oxides (NO_x) gasses, respectively, when they are incinerated. Accordingly, inorganic pigments composed of oxides are considered to be ideal materials from a practical perspective.

A number of oxidic compounds have been already reported as new environmentally friendly inorganic pigments [7−27]. The research group, to which the present author belongs, has also been working toward the synthesis of several environmentally friendly yellow pigments to meet environmental requirements and the demands of safety-oriented producers [28−34]. Unfortunately, the color properties of these pigments are not enough in comparison

with those of the conventional toxic ones. In addition, $YIn_{1-x}Mn_xO_3$ compounds have also been reported as environmentally friendly inorganic pigments with the potential to give brilliant blue color [35, 36]. However, one of the constituent elements, indium (In), has the potential for causing interstitial lung disease [37].

In order to develop the novel environmentally friendly inorganic pigments that can substitute for the conventional toxic materials, it is essential to choose the base materials which are composed of only nontoxic elements and/or have already been identified as nontoxic compounds. Of course, the other constituent elements also have to be nontoxic and safe. Based on the above concept, in this work, novel and environmentally friendly inorganic yellow, red, and blue pigments with high color performance were synthesized and their color properties were characterized from the view point of possible ecologically friendly inorganic materials.

The present work of this thesis consists of the following three chapters.

In **Chapter 1**, novel yellow pigments, $Bi_{1-x-y-z}Ca_xZn_yLa_zVO_{4-(x+y)/2}$ ($0.04 \leq x \leq 0.12$; $0.01 \leq y \leq 0.05$; $0.01 \leq z \leq 0.10$), are described. These pigments were synthesized to further enhance the yellow hue of a $Bi_{0.90}Ca_{0.08}Zn_{0.02}VO_{3.950}$ pigment, which was previously reported by our research group.

In **Chapter 2**, novel red pigments, $(Bi_{1-x-y}Zr_xAl_y)_4V_2O_{11+\delta}$ ($0 \leq x \leq 0.15$; $0 \leq y \leq 0.10$), in which a portion of bismuth ions in the $Bi_4V_2O_{11}$ lattice was substituted with Zr^{4+} and/or Al^{3+} ions, are described.

In **Chapter 3**, novel blue pigments, $(Ca_{1-x}Eu_x)_3Sc_2Si_3O_{12+\delta}$ ($0 \leq x \leq 0.10$), are described. The composition and the synthesis conditions were optimized to produce the most vivid blue hue.

List of Publications

1. Novel Environment-friendly Yellow Pigments Based on (Bi, La)VO_4

   Wendusu, Ken-ichi Ikawa, Toshiyuki Masui, Nobuhito Imanaka

   Chemistry Letters, 2011, **40**, 792−794.

2. Environmentally Friendly Inorganic Red Pigments Based on Bismuth Oxide

   Wendusu, Toshiyuki Masui, Nobuhito Imanaka

   Chemistry Letters, 2012, **41**, 1616−1618.

3. Novel Environmentally Friendly Inorganic Blue Pigments Based on Amorphous Tungsten Oxyphosphate

   Wendusu, Ayaka Hosoya, Toshiyuki Masui, Nobuhito Imanaka

   Chemistry Letters, 2013, **42**, 906−908.

4. Novel Environmentally Friendly Inorganic Blue Pigments Based on Calcium Scandium Silicate Garnet

   Wendusu, Taihei Honda, Toshiyuki Masui, Nobuhito Imanaka

   Chemistry Letters, 2013, **42**, 1562−1564.

5. Novel Environmentally Friendly (Bi, Ca, Zn, La)VO_4 Inorganic Yellow Pigments

   Wendusu, Taihei Honda, Toshiyuki Masui, Nobuhito Imanaka

   RSC Advances, 2013, **3**, 24941−24945.

6. Novel Environment-friendly Inorganic Red Pigments Based on (Bi, Er, Y, Fe)$_2O_3$ Solid Solutions

   Wendusu, Toshiyuki Masui, Nobuhito Imanaka

   Journal of Asian Ceramic Societies, 2014, **2**, 195−198.

7. Novel Environmental Friendly Inorganic Red Pigments Based on $Bi_4V_2O_{11}$

   Wendusu, Atsunori Shiraishi, Naoki Takeuchi, Toshiyuki Masui, Nobuhito Imanaka

   in preparation.

Supplementary Publications

1. Novel and Environmentally Friendly (Bi, Ca, Zn)VO_4 Yellow Pigments

   Toshiyuki Masui, Taihei Honda, **Wendusu**, Nobuhito Imanaka

   Dyes and Pigments, 2013, **99**, 636−641.

2. Novel Environmentally Friendly Inorganic Yellow Pigments Based on CeO_2-SiO_2-Al_2O_3-Bi_2O_3

   Wendusu, Daisuke Kato, Toshiyuki Masui, Nobuhito Imanaka

   Bulletin of the Chemical Society of Japan, 2013, **86**, 283−288.

3. Novel Environmentally Friendly Inorganic Red Pigments Based on Calcium Bismuth Oxides

   Wendusu, Tetsuro Yoshida, Toshiyuki Masui, Nobuhito Imanaka

   Journal of Advanced Ceramics, 2015, **4(1)**, 39−45.

Chapter 1

Synthesis of Novel Inorganic Yellow Pigments Based on Bismuth Vanadate ($BiVO_4$)

1.1 Introduction

As mentioned in the General Introduction, this chapter describes synthesis of novel environmentally friendly yellow pigments. For the synthesis of such pigments, bismuth vanadate ($BiVO_4$) was selected as a base material. This compound has already been known as an environmentally friendly inorganic yellow pigment for industrial uses [1, 2], but its yellow color is inferior to those of the conventional toxic ones. Accordingly, this material cannot be a perfect substitute for the conventional toxic pigments.

Bismuth vanadate can form three polymorphic phases: tetragonal dreyerite, monoclinic clinobisvanite, and orthorhombic pucherite [38]. Among them, the monoclinic $BiVO_4$ is thermodynamically stable and vivid yellow [39]. The coloring mechanism of monoclinic $BiVO_4$ originates in a charge transfer transition from a valence band (VB) of a hybrid orbital of Bi_{6s} and O_{2p} to a conduction band (CB) of V_{3d} in the band structure [38, 40−43]. Therefore, it is expected that the color of $BiVO_4$ can be tuned by introducing other elements into the $BiVO_4$ lattice to control the lattice size, because the extent of the orbital hybridization in the Bi_{6s}−O_{2p} valence band should depend on the interionic distance between Bi^{3+} and O^{2-}.

Based on this concept, $Bi_{1-x}La_xVO_4$ ($0 \leq x \leq 0.15$) solid solutions were synthesized, and it was clarified that a $Bi_{0.90}La_{0.10}VO_4$ pigment exhibited the most yellowish hue (b^* = +86.6 in the CIE $L^*a^*b^*$ system) among them. The hybridization degree of the valence band

was increased by the doping of smaller La^{3+} (ionic radius: 0.116 nm) [44] ions into the Bi^{3+} (ionic radius: 0.117 nm) [44] sites of the $BiVO_4$ lattice to generate lattice shrinkage. As a result, the width of the valence band was increased, leading to the decrease in the bandgap energy. However, a small amount of the tetragonal phase, which shows murky yellowish hue [39], was formed as an impurity, when an excess amount of La^{3+} was doped ($x = 0.15$).

Furthermore, $Bi_{1-x-y}Ca_xZn_yVO_{4-(x+y)/2}$ ($0 \leq x \leq 0.10$; $0 \leq y \leq 0.10$) solid solutions were also successfully synthesized. In the solid solutions, the lattice volumes were shrunk in comparison with that of $BiVO_4$ and oxide anion vacancies were generated by the charge compensation mechanism, because trivalent Bi^{3+} (ionic radius: 0.117 nm) [44] was substituted with smaller divalent Ca^{2+} (ionic radius: 0.112 nm) [44] and/or Zn^{2+} (ionic radius: 0.090 nm) [44]. Although a single-phase monoclinic structure was observed for all solid solutions, overproduction of the oxide anion vacancies in the lattice caused the decrease in the yellow hue. Therefore, the composition was optimized to liven the yellow color, and, as a result, a $Bi_{0.90}Ca_{0.08}Zn_{0.02}VO_{3.950}$ pigment showed the most vivid yellow hue with a yellowness value (b^* in the CIE $L^*a^*b^*$ system) of +91.6.

From the results mentioned above, the following findings were obtained.

(1) The lattice shrinkage of $BiVO_4$ by the introduction of trivalent cation into the lattice is effective to increase the yellowness, but the excess doping induces the formation of the tetragonal impurity phase.

(2) The lattice shrinkage of $BiVO_4$ accompanying with the formation of oxide anion vacancies is also effective to enhance the yellow color without the production of the tetragonal impurity phase, but the introduction of an excess amount of the vacancies has the opposite effect to produce vivid yellow color.

Taking into consideration of these findings, it is reasonable to expect that the yellowness of $Bi_{1-x-y}Ca_xZn_yVO_{4-(x+y)/2}$ could be improved by the introduction of La^{3+} to

further shrink the lattice without the overproduction of the oxide anion vacancies. In this chapter, therefore, synthesis and characterization of novel $Bi_{1-x-y-z}Ca_xZn_yLa_zVO_{4-(x+y)/2}$ ($0.04 \leq x \leq 0.12$; $0.01 \leq y \leq 0.05$; $0.01 \leq z \leq 0.10$) yellow pigments are described. The color properties of the samples are characterized and the concentrations of La^{3+}, Ca^{2+}, and Zn^{2+} are optimized to produce the most vivid yellow hue.

1.2 Experimental Procedure

The $Bi_{1-x-y-z}Ca_xZn_yLa_zVO_{4-(x+y)/2}$ ($0.04 \leq x \leq 0.12$; $0.01 \leq y \leq 0.05$; $0.01 \leq z \leq 0.10$) pigments were synthesized by an evaporation to dryness method. A stoichiometric mixture of 0.5 mol dm^{-3} $Bi(NO_3)_3$, 0.1 mol dm^{-3} $Ca(NO_3)_2$, 0.1 mol dm^{-3} $Zn(NO_3)_2$, and 0.1 mol dm^{-3} $La(NO_3)_3$ aqueous solutions was added to 30 cm^3 of nitric acid solution (3.0 mol dm^{-3}), in which 1.08 g of NH_4VO_3 was dissolved. The pH of the aqueous mixture was adjusted to 6.5 by dropwise addition of an aqueous solution of ammonia (5%). After stirring at room temperature for 1 h, the mixed solution was heated at 180 ºC until the solvent was vaporized. The resultant solid was then ground in an agate mortar and finally calcined at 650 ºC for 6 h in a flow of air to afford the product. The obtained pigments were gently ground in an agate mortar before characterization.

The samples were characterized by X-ray powder diffraction (XRD; Rigaku, SmartLab) with Cu-Kα radiation (40 kV and 30 mA) to identify the crystal structure. The lattice volumes of the samples were calculated from the peak angles in the XRD patterns, which were refined using α-Al_2O_3 as a standard. The lattice strain into the samples was estimated using the Williamson-Hall equation, $\beta \cos\theta/\lambda = 2\varepsilon \sin\theta/\lambda + K/D$ (β: full width at half maximum (FWHM); λ: wavelength of the X-ray, 0.154178 nm; ε: lattice strain; K: Scherrer constant, 1.05; D: crystallite diameter) [45]. X-ray fluorescence spectroscopy (XRF; Rigaku, ZSX-100e) measurements were used to analyze the composition of the samples. The

optical reflectance was measured with a UV-Vis spectrometer (Shimadzu, UV-2600) using barium sulfate as a reference. The bandgap energies of the samples were determined from the absorption edge of the absorbance spectra represented by the Kubelka–Munk function, $f(R) = (1 - R)^2/2R$, where R is reflectance [46, 47]. The color properties of the samples were evaluated in terms of the CIE $L^*a^*b^*CH°$ system using a chromometer (Konica-Minolta, CR-300). The L^* parameter represents the brightness or darkness of a color relative to a neutral grey scale, and the a^* (the red–green axis) and b^* (the yellow–blue axis) parameters express the color qualitatively. The parameters C (chroma) and $H°$ represent saturation of the color and the hue angle, respectively. The chroma (C) is defined as $C = [(a^*)^2 + (b^*)^2]^{½}$. The hue angle ($H°$) ranges from 0 to 360° and is calculated using the formula, $H° = \tan^{-1}(b^*/a^*)$. Raman spectra were obtained using a Jasco NRS-3100 spectrometer with a green laser (532 nm) as an excitation source, operated at a power of 100 mW, and a CCD detector.

1.3 Results and Discussion

1.3.1 $Bi_{0.90-z}Ca_{0.08}Zn_{0.02}La_zVO_{3.950}$ ($0 \le z \le 0.10$) pigments

XRD patterns of the $Bi_{0.90-z}Ca_{0.08}Zn_{0.02}La_zVO_{3.950}$ ($0 \le z \le 0.10$) samples are shown in **Figure 1.1**. The monoclinic $BiVO_4$ structure was obtained in a single-phase form for the samples in which the La^{3+} content was 5 mol% and less, and there were no extra lines due to other compounds or impurity phases. In contrast, for the samples in which the La^{3+} concentration was more than 5 mol%, a tetragonal $BiVO_4$ structure was observed as an impurity phase in addition to the monoclinic structure.

Figure 1.2 depicts the La^{3+} content dependence of the monoclinic lattice volume in the $Bi_{0.90-z}Ca_{0.08}Zn_{0.02}La_zVO_{3.950}$ ($0 \le z \le 0.10$) pigments. The monoclinic lattice volume of the samples monotonously decreased with the increase in the amount of La^{3+} in the single-phase region ($0 \le z \le 0.05$), because the ionic radius of La^{3+} (0.116 nm) [44] is smaller

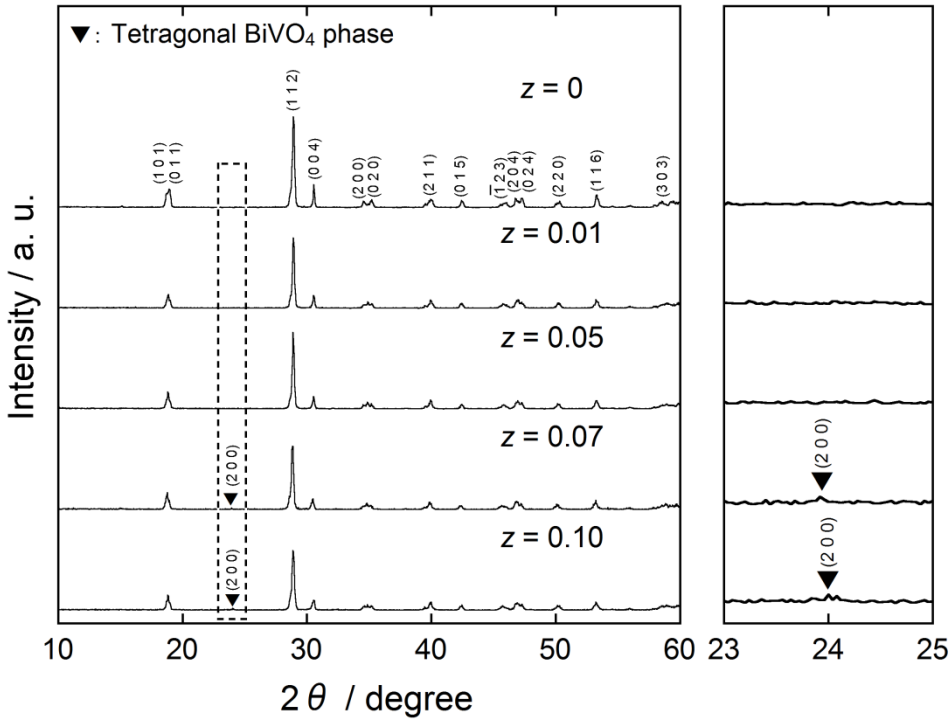

Figure 1.1 XRD patterns of the $Bi_{0.90-z}Ca_{0.08}Zn_{0.02}La_zVO_{3.950}$ ($0 \leq z \leq 0.10$) samples.

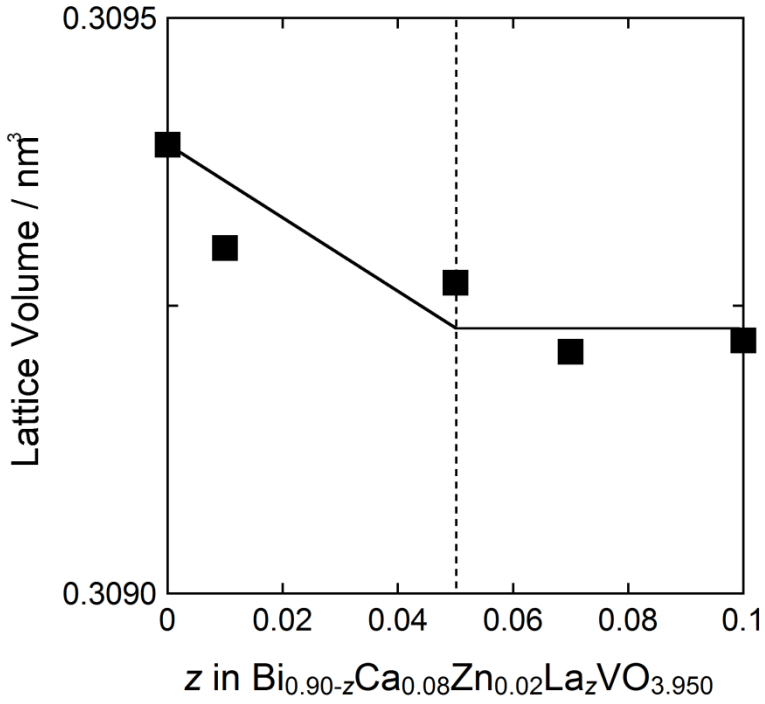

Figure 1.2 Dependence of the monoclinic lattice volume on the La^{3+} content in the $Bi_{0.90-z}Ca_{0.08}Zn_{0.02}La_zVO_{3.950}$ ($0 \leq z \leq 0.10$) pigments.

than that of Bi^{3+} (0.117 nm) [44]. However, the lattice volume of the samples became nearly constant in the two-phase region ($0.05 < z \leq 0.10$). These results indicated that solid solutions with a single-phase monoclinic $BiVO_4$ structure were successfully formed and the solubility limit of La^{3+} ions was approximately 5 mol% in this system.

Figure 1.3 illustrates UV-Vis diffuse reflectance spectra for the $Bi_{0.90-z}Ca_{0.08}Zn_{0.02}La_zVO_{3.950}$ ($0 \leq z \leq 0.10$) samples. Strong optical absorption behavior was observed for all samples at wavelengths shorter than 500 nm, including the blue light region (435 − 480 nm). These samples are yellow, because blue is the complementary color of yellow. The wavelength of absorption edge depended on the sample composition, and the strongest absorption in the blue region was observed for $Bi_{0.85}Ca_{0.08}Zn_{0.02}La_{0.05}VO_{3.950}$.

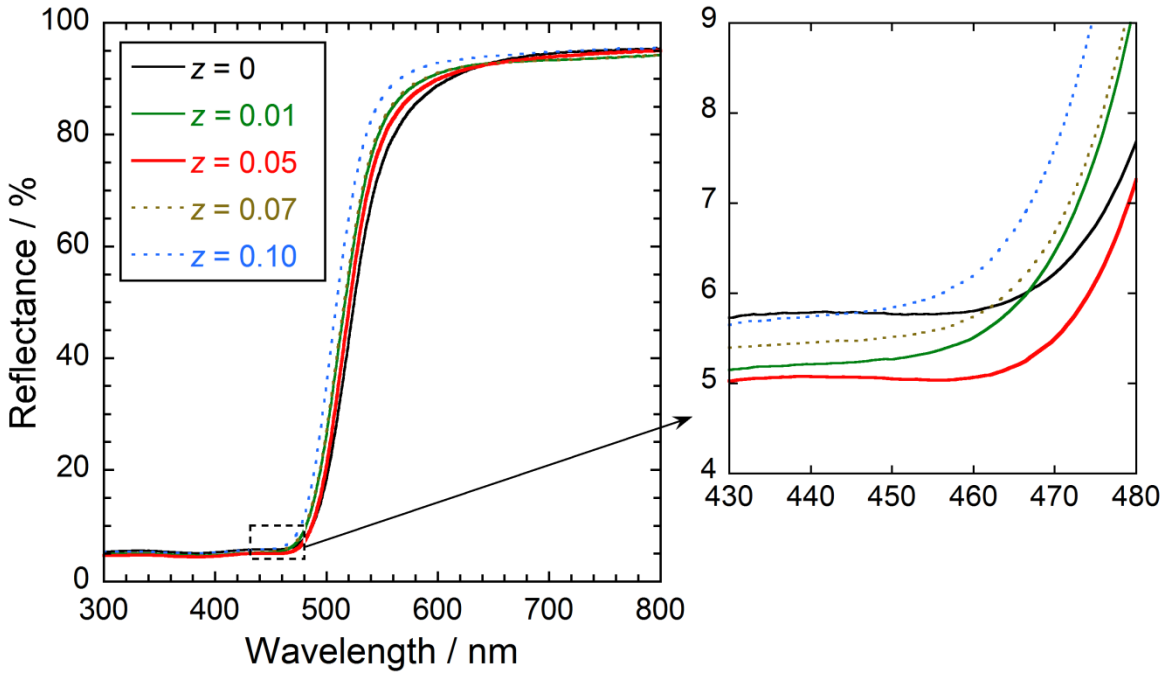

Figure 1.3 UV-Vis diffuse reflectance spectra for the $Bi_{0.90-z}Ca_{0.08}Zn_{0.02}La_zVO_{3.950}$ ($0 \leq z \leq 0.10$) samples.

The CIE $L^*a^*b^*CH^o$ color coordinate data and bandgap energies (E_g) of the $Bi_{0.90-z}Ca_{0.08}Zn_{0.02}La_zVO_{3.950}$ ($0 \leq z \leq 0.10$) pigments are summarized in **Table 1.1**. All samples are yellow, because the hue angle ($H°$) parameters fall in the yellow region ($70^o < H° < 105^o$). The b^* value corresponding to yellow chromaticity and the color saturation parameter (C) depend on the concentration of La^{3+} and the $Bi_{0.85}Ca_{0.08}Zn_{0.02}La_{0.05}VO_{3.950}$ pigment has the highest b^* and C values at +93.5 and 93.8, respectively. The decrease in these values in the samples with La^{3+} content of more than 5 mol% is attributed to the formation of the impurity tetragonal $BiVO_4$ phase, as seen in **Figure 1.1**, which is murky yellow [39].

Table 1.1 CIE $L^*a^*b^*CH^o$ color coordinate data and bandgap energies (E_g) of the pigments

Pigments	L^*	a^*	b^*	C	H^o	E_g / eV
$Bi_{0.90}Ca_{0.08}Zn_{0.02}VO_{3.950}$	87.7	−4.36	+91.6	91.7	92.7	2.42
$Bi_{0.89}Ca_{0.08}Zn_{0.02}La_{0.01}VO_{3.950}$	89.2	−7.27	+92.4	92.7	94.5	2.42
$Bi_{0.85}Ca_{0.08}Zn_{0.02}La_{0.05}VO_{3.950}$	89.0	−6.82	+93.5	93.8	94.2	2.42
$Bi_{0.83}Ca_{0.08}Zn_{0.02}La_{0.07}VO_{3.950}$	90.1	−8.80	+91.0	91.4	95.5	2.42
$Bi_{0.80}Ca_{0.08}Zn_{0.02}La_{0.10}VO_{3.950}$	92.0	−12.7	+89.2	90.1	98.1	2.44

1.3.2 $Bi_{0.93-x}Ca_xZn_{0.02}La_{0.05}VO_{3.990-x/2}$ and $Bi_{0.87-y}Ca_{0.08}Zn_yLa_{0.05}VO_{3.960-y/2}$

As mentioned in the previous section, the optimum La^{3+} concentration that exhibited the highest yellow hue was 5 mol% in the $Bi_{0.90-z}Ca_{0.08}Zn_{0.02}La_zVO_{3.950}$ system. In this section, the concentrations of Ca^{2+} and Zn^{2+} were adjusted minutely to determine the optimum composition that gave the most vivid yellow hue for the samples in which the concentration of La^{3+} was fixed at 5 mol%.

Accordingly, $Bi_{0.93-x}Ca_xZn_{0.02}La_{0.05}VO_{3.990-x/2}$ and $Bi_{0.87-y}Ca_{0.08}Zn_yLa_{0.05}VO_{3.960-y/2}$ samples were synthesized and their color properties were evaluated. **Figure 1.4** shows the XRD patterns of the $Bi_{0.93-x}Ca_xZn_{0.02}La_{0.05}VO_{3.990-x/2}$ (a) and $Bi_{0.87-y}Ca_{0.08}Zn_yLa_{0.05}VO_{3.960-y/2}$ (b) samples. A single-phase monoclinic $BiVO_4$ structure was obtained for all the samples, and there were no diffraction peaks due to any impurities in the patterns. **Figure 1.5** shows the monoclinic lattice volume of the $Bi_{0.93-x}Ca_xZn_{0.02}La_{0.05}VO_{3.990-x/2}$ (a) and $Bi_{0.87-y}Ca_{0.08}Zn_yLa_{0.05}VO_{3.960-y/2}$ (b) samples. The lattice volume decreased monotonously with increasing Ca^{2+} or Zn^{2+} concentration, because the ionic radii of Ca^{2+} (0.112 nm) [44] and Zn^{2+} (0.090 nm) [44] are smaller than that of Bi^{3+} (0.117 nm) [44]. These results indicate that solid solutions of a single monoclinic $BiVO_4$ phase were successfully formed for all samples.

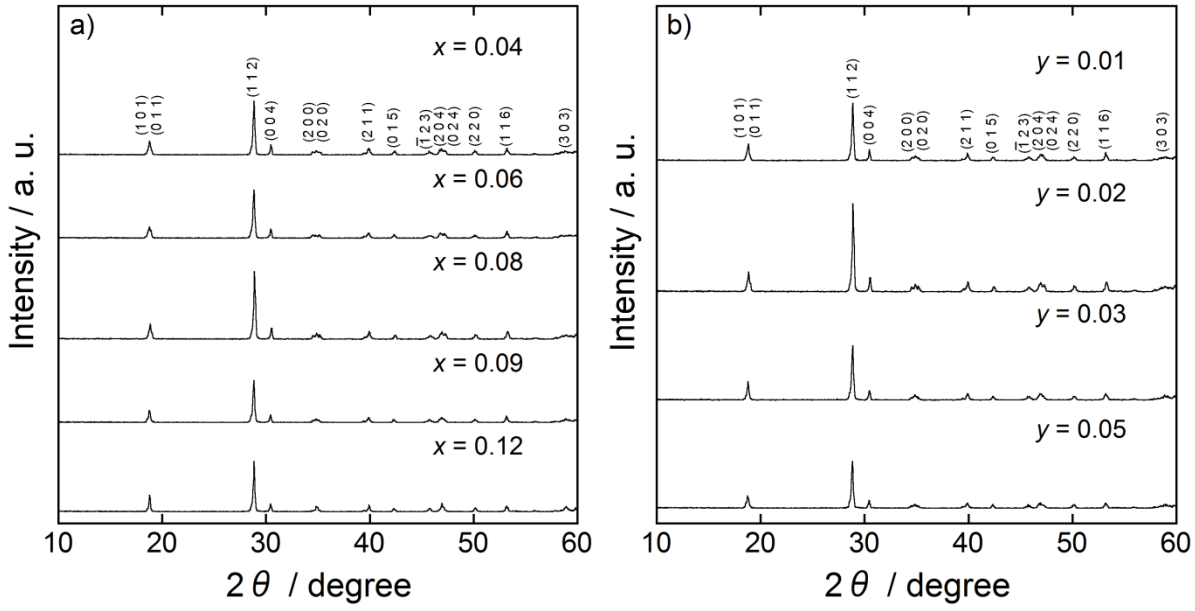

Figure 1.4 XRD patterns of the $Bi_{0.93-x}Ca_xZn_{0.02}La_{0.05}VO_{3.990-x/2}$ (a) and $Bi_{0.87-y}Ca_{0.08}Zn_yLa_{0.05}VO_{3.960-y/2}$ (b) samples.

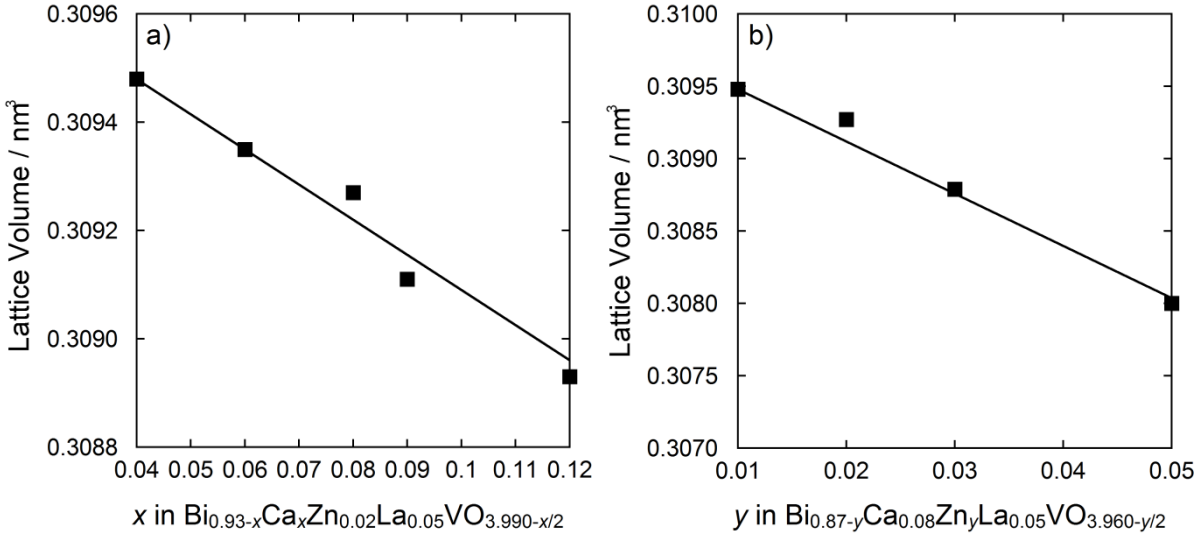

Figure 1.5 Dependence of the monoclinic lattice volume on the composition in the $Bi_{0.93-x}Ca_xZn_{0.02}La_{0.05}VO_{3.990-x/2}$ (a) and $Bi_{0.87-y}Ca_{0.08}Zn_yLa_{0.05}VO_{3.960-y/2}$ (b) samples.

Figure 1.6 illustrates the UV-Vis diffuse reflectance spectra of the $Bi_{0.93-x}Ca_xZn_{0.02}La_{0.05}VO_{3.990-x/2}$ (a) and $Bi_{0.87-y}Ca_{0.08}Zn_yLa_{0.05}VO_{3.960-y/2}$ (b) samples. The wavelength of the reflectance edge depended on the sample composition, and the maximum absorption in blue light region (435 − 480 nm) was observed at the composition of $Bi_{0.85}Ca_{0.08}Zn_{0.02}La_{0.05}VO_{3.950}$. The CIE $L^*a^*b^*CH^o$ color coordinate data and bandgap energies (E_g) of the $Bi_{0.93-x}Ca_xZn_{0.02}La_{0.05}VO_{3.990-x/2}$ and $Bi_{0.87-y}Ca_{0.08}Zn_yLa_{0.05}VO_{3.960-y/2}$ pigments are tabulated in **Table 1.2**, with those of the commercially available $BiVO_4$ (Dainichiseika Color & Chemicals Mfg., IRGACOLOR YELLOW 2GLMA) and $PbCrO_4$ (NIC NEO5GS) pigments for comparison. The highest b^* and C values were obtained for the $Bi_{0.85}Ca_{0.08}Zn_{0.02}La_{0.05}VO_{3.950}$ pigment (b^* = +93.5, C = 93.8), as in the UV-Vis diffuse reflectance measurement. Although the yellowness value and the color saturation parameter for the $Bi_{0.85}Ca_{0.08}Zn_{0.02}La_{0.05}VO_{3.950}$ pigment fall just one step short of those for the toxic $PbCrO_4$ (b^* = +96.5, C = 96.5) pigment, they are significantly greater than those for the environmentally friendly $BiVO_4$ pigment (b^* = +80.3, C = 81.8).

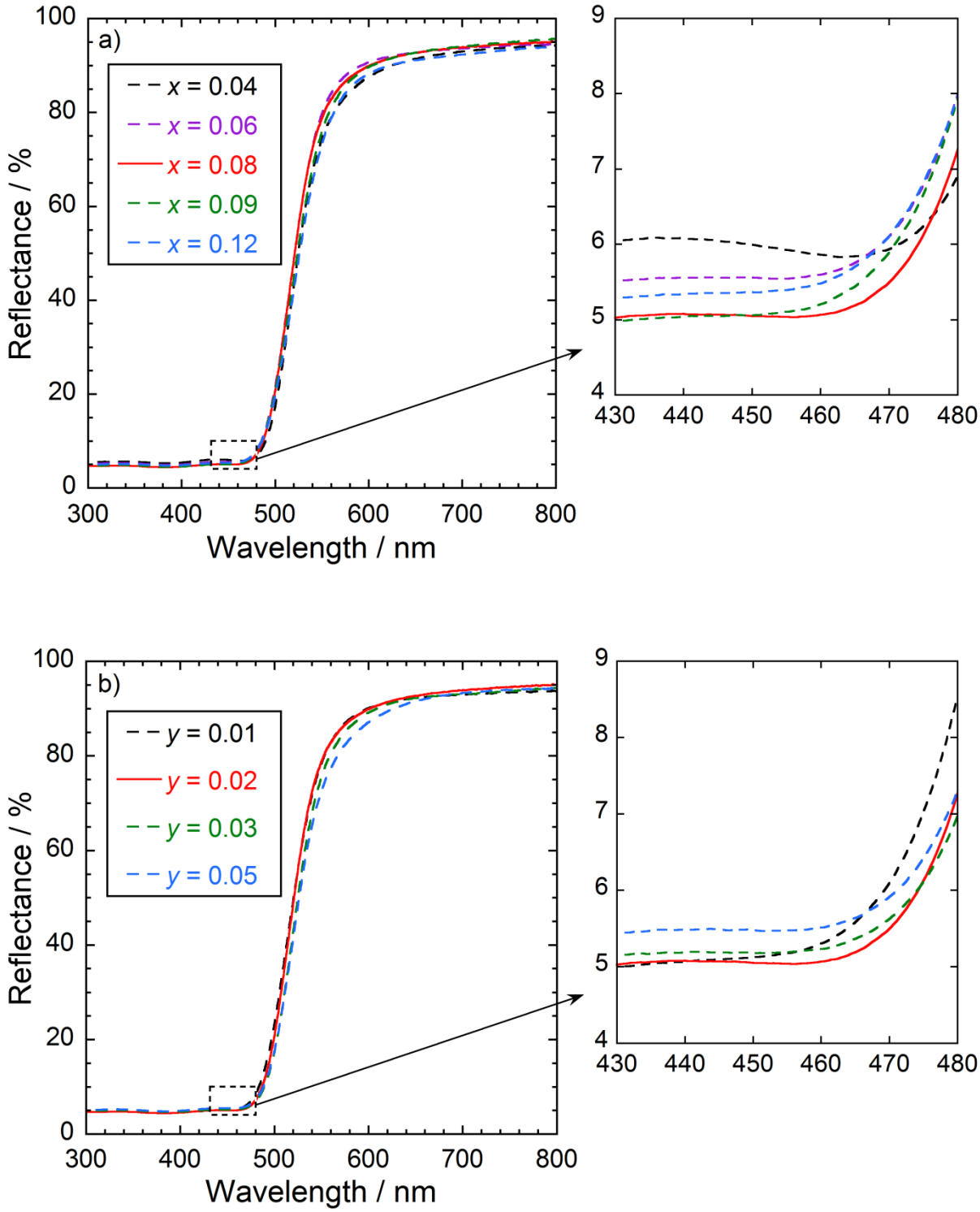

Figure 1.6 UV-Vis diffuse reflectance spectra of the $Bi_{0.93-x}Ca_xZn_{0.02}La_{0.05}VO_{3.990-x/2}$ (a) and $Bi_{0.87-y}Ca_{0.08}Zn_yLa_{0.05}VO_{3.960-y/2}$ (b) samples.

Table 1.2 CIE $L^*a^*b^*CH^o$ color coordinate data and bandgap energies (E_g) of the pigments

Pigments	L^*	a^*	b^*	C	H^o	E_g / eV
$Bi_{0.90}Ca_{0.08}Zn_{0.02}VO_{3.950}$	87.7	−4.36	+91.6	91.7	92.7	2.42
$Bi_{0.89}Ca_{0.04}Zn_{0.02}La_{0.05}VO_{3.970}$	87.4	−4.05	+89.8	89.9	92.6	2.44
$Bi_{0.87}Ca_{0.06}Zn_{0.02}La_{0.05}VO_{3.960}$	89.8	−7.72	+91.0	91.3	94.8	2.43
$Bi_{0.85}Ca_{0.08}Zn_{0.02}La_{0.05}VO_{3.950}$	89.0	−6.82	+93.5	93.8	94.2	2.42
$Bi_{0.84}Ca_{0.09}Zn_{0.02}La_{0.05}VO_{3.945}$	88.4	−3.39	+93.1	93.2	92.1	2.42
$Bi_{0.81}Ca_{0.12}Zn_{0.02}La_{0.05}VO_{3.930}$	87.8	−2.11	+91.7	91.7	91.3	2.41
$Bi_{0.86}Ca_{0.08}Zn_{0.01}La_{0.05}VO_{3.955}$	89.5	−5.53	+93.0	93.2	93.4	2.43
$Bi_{0.85}Ca_{0.08}Zn_{0.02}La_{0.05}VO_{3.950}$	89.0	−6.82	+93.5	93.8	94.2	2.42
$Bi_{0.84}Ca_{0.08}Zn_{0.03}La_{0.05}VO_{3.945}$	87.1	−3.86	+93.1	93.2	92.4	2.41
$Bi_{0.82}Ca_{0.08}Zn_{0.05}La_{0.05}VO_{3.935}$	86.9	−2.28	+91.2	91.2	91.4	2.40
Commercially available $BiVO_4$	93.3	−15.7	+80.3	81.8	101.1	2.51
Commercially available $PbCrO_4$	89.9	+1.12	+96.5	96.5	89.3	2.38

As mentioned above, the highest b^* value was obtained for the $Bi_{0.85}Ca_{0.08}Zn_{0.02}La_{0.05}VO_{3.950}$ pigment (b^* = +93.5). However, its bandgap energy was equivalent to that of non-doped $Bi_{0.90}Ca_{0.08}Zn_{0.02}VO_{3.950}$. To clarify the reason for that, Raman spectra of the previous $Bi_{0.90}Ca_{0.08}Zn_{0.02}VO_{3.950}$ and present $Bi_{0.85}Ca_{0.08}Zn_{0.02}La_{0.05}VO_{3.950}$ pigments were measured as illustrated in **Figure 1.7**. The spectrum of the previous $Bi_{0.90}Ca_{0.08}Zn_{0.02}VO_{3.950}$ shows a strong band at 817 cm^{-1}, which is attributed to the ν_1 symmetric stretching mode of VO_4 units [48], and small bands at 336 and 365 cm^{-1} that correspond to the ν_2 bending modes of VO_4 units [48]. In contrast, for the spectrum of the

$Bi_{0.85}Ca_{0.08}Zn_{0.02}La_{0.05}VO_{3.950}$ pigment, there is an additional band at 712 cm^{-1}, which is assigned to the ν_3 asymmetric stretching mode of VO_4 units [48]. These results indicate that local strain in the crystal structure was generated by doping La^{3+} ions into the $Bi_{0.90}Ca_{0.08}Zn_{0.02}VO_{3.950}$ lattice. In fact, the local strain in the $Bi_{0.85}Ca_{0.08}Zn_{0.02}La_{0.05}VO_{3.950}$ lattice was estimated to be 0.198%, while that in the $Bi_{0.90}Ca_{0.08}Zn_{0.02}VO_{3.950}$ lattice was about 0.057%, from the Williamson-Hall plots illustrated in **Figure 1.8**. This is probably one of the reasons why $Bi_{0.85}Ca_{0.08}Zn_{0.02}La_{0.05}VO_{3.950}$ has more vivid yellow hue than $Bi_{0.90}Ca_{0.08}Zn_{0.02}VO_{3.950}$ even though both of them have the same bandgap energies.

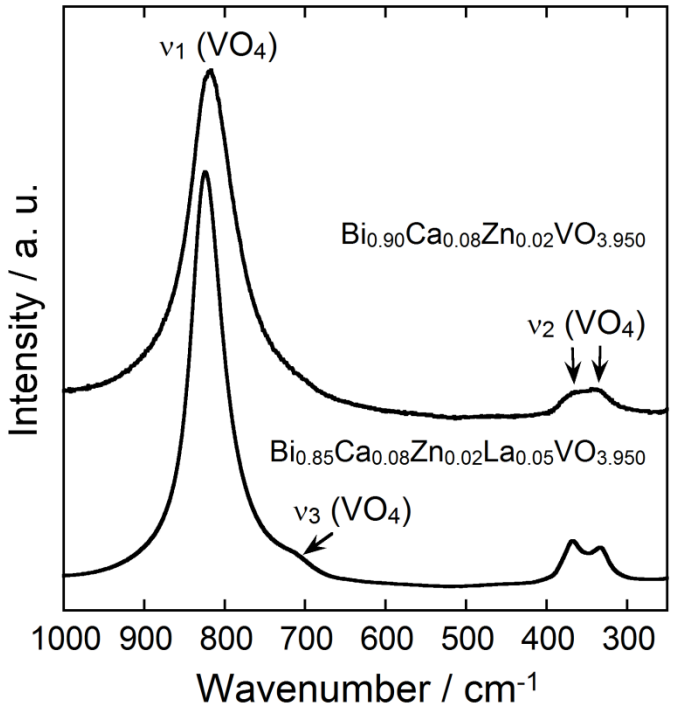

Figure 1.7 Raman spectra of the $Bi_{0.90}Ca_{0.08}Zn_{0.02}VO_{3.950}$ and $Bi_{0.85}Ca_{0.08}Zn_{0.02}La_{0.05}VO_{3.950}$ pigments.

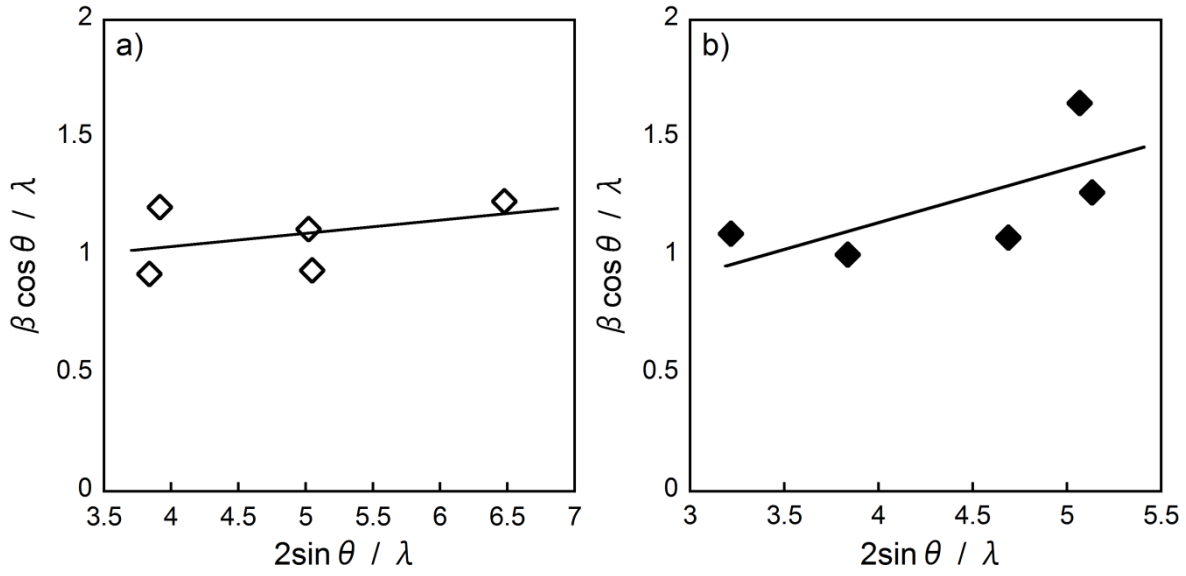

Figure 1.8 Williamson-Hall plots of the $Bi_{0.90}Ca_{0.08}Zn_{0.02}VO_{3.950}$ (a) and $Bi_{0.85}Ca_{0.08}Zn_{0.02}La_{0.05}VO_{3.950}$ (b) pigments.

1.4 Conclusion

$Bi_{1-x-y-z}Ca_xZn_yLa_zVO_{4-(x+y)/2}$ ($0.04 \leq x \leq 0.12$; $0.01 \leq y \leq 0.05$; and $0.01 \leq z \leq 0.10$) pigments were successfully synthesized as novel environmentally friendly inorganic yellow pigments. The color of the pigments was dependent on the concentrations of Ca^{2+}, Zn^{2+}, and La^{3+}. The most vivid yellowness was obtained for $Bi_{0.85}Ca_{0.08}Zn_{0.02}La_{0.05}VO_{3.950}$, which has CIE $L^*a^*b^*$ color parameters of $L^* = 89.0$, $a^* = -6.82$, and $b^* = +93.5$. The b^* value is markedly higher than that of a commercially available $BiVO_4$ pigment ($b^* = +80.3$). Since $BiVO_4$ has been already known as an environmentally friendly inorganic yellow pigment, and Ca, Zn, and La are also nontoxic and safe elements, the present pigments should be suitable alternatives for the conventional toxic ones.

Chapter 2

Synthesis of Novel Inorganic Red Pigments Based on Bismuth Vanadate ($Bi_4V_2O_{11}$)

2.1 Introduction

In this chapter, novel environmentally friendly inorganic red pigments are described. At the beginning, bismuth oxide (Bi_2O_3) was chosen as a base material because this compound has already been reported to be nontoxic and insoluble [49]. Although Bi_2O_3 is a pale yellow compound, the color was altered to be reddish by the change in the lattice size and the band structure when Er^{3+}, Y^{3+}, and Fe^{3+} ions were dissolved into the Bi_2O_3 lattice. Among the Er^{3+}, Y^{3+}, and Fe^{3+}-doped pigments synthesized, the most brilliant red hue was obtained for $((Bi_{0.72}Er_{0.04}Y_{0.24})_{0.80}Fe_{0.20})_2O_3$ (a^* = +33.1 in the CIE $L^*a^*b^*$ system). The red hue of this pigment surpassed that of a commercially available Fe_2O_3 pigment (a^* = +28.9), but the difference was small. Accordingly, it is highly required to synthesize new red pigments with more reddish hue.

Because of this situation, bismuth vanadate ($Bi_4V_2O_{11}$) with orthorhombic structure (space group: *Aba*2 [50, 51]) came to the forefront as a new base material. The structure of orthorhombic $Bi_4V_2O_{11}$ consists of Bi_2O_2 layers interleaved with vanadium oxide sheets, which are composed of edge-shared VO_4 and VO_6 units. However, half of the VO_6 units contain a blank oxide anion site, and accordingly, the VO_4 layer acts as $VO_{3.5}$ [51].

As is the case with monoclinic $BiVO_4$ described in **Chapter 1**, the coloring mechanism of the $Bi_4V_2O_{11}$ is also based on a charge transfer transition from a hybrid Bi_{6s}−O_{2p} orbital to V_{3d} orbital in the band structure. Furthermore, the mean interionic distance

between Bi^{3+} and O^{2-} in the $Bi_4V_2O_{11}$ lattice is approximately 0.23 nm [51, 52], which is shorter than that in the monoclinic $BiVO_4$ lattice (0.2467 nm) [53]. Accordingly, it is expected that the hybridization degree of the valence band in $Bi_4V_2O_{11}$ is higher than that in $BiVO_4$, and consequently, bandgap energy of $Bi_4V_2O_{11}$ became smaller than that of $BiVO_4$. Therefore, it is expected that orthorhombic $Bi_4V_2O_{11}$ can serve as a base material for novel red pigments, by absorbing visible light in the longer wavelengths region.

In **Chapter 1**, it has been elucidated that lattice shrinkage positively affects the color properties by modulating the width of valence band, whereas, an excess amount of oxide anion vacancies gives a negative effect on the color properties. In accordance with these findings, in the study described in this chapter, blank oxide anion sites in the $Bi_4V_2O_{11}$ lattice were filled by the synthesis in a flow of oxygen, accompanying with the oxidation state change of a part of bismuth ions from Bi^{3+} to Bi^{5+}. Furthermore, smaller Zr^{4+} (ionic radius: 0.072 nm) and Al^{3+} (ionic radius: 0.0535 nm) ions were doped into the Bi^{3+} (ionic radius: 0.103 nm) and Bi^{5+} (ionic radius: 0.076 nm) [44] sites of the lattice. In this chapter, therefore, novel $(Bi_{1-x-y}Zr_xAl_y)_4V_2O_{11+\delta}$ ($0 \leq x \leq 0.15$; $0 \leq y \leq 0.10$) red pigments are described. The color properties of the samples were characterized, and, the doping effects of Zr^{4+} and Al^{3+} were revealed.

2.2 Experimental Procedure

The $(Bi_{1-x-y}Zr_xAl_y)_4V_2O_{11+\delta}$ ($0 \leq x \leq 0.15$; $0 \leq y \leq 0.10$) pigments were synthesized by a conventional solid state reaction method. Stoichiometric amount of Bi_2O_3, ZrO_2, Al_2O_3, and V_2O_5 powders were mixed in an agate mortar. After mechanically mixed with a planetary-type ball-milling apparatus (PULVERISETTE 7, Fritsch GmbH), the homogenous mixture was calcined at 800 ºC for 10 h in a flow of air or pure O_2. The obtained samples were gently ground in an agate mortar before characterization.

The crystal structures of the samples were identified by X-ray powder diffraction (XRD; Rigaku SmartLab) using Cu-Kα radiation (40 kV, 30 mA). The compositions of the samples were analyzed by X-ray fluorescence spectrometer (XRF, Rigaku Supermini200), and it was confirmed that they were in good agreement with the theoretical values within the experimental errors. X-ray photoelectron spectroscopy (XPS; ULVAC 5500MT) was performed at room temperature with Mg-Kα radiation (1253.6 eV) without Ar etching. The effect of charging on the binding energies was corrected with respect to the C 1s peak at 284.6 eV.

Bi L_{III} XANES (X-ray absorption near-edge structure) spectra of the samples were measured in the transmission mode using the BL−11 beam line at SAGA Light Source (SAGA-LS). A Si (111) double-crystal monochromator was employed to monochromize the synchrotron radiation. The I_0 and I ionization chambers were filled with $N_2$85%−Ar15% mixture gas and pure Ar gas, respectively. XANES spectrum of α-Bi_2O_3 was also measured as a standard material.

Optical reflectance spectra of the samples were measured using a UV-Vis spectrometer (Shimadzu UV-2600) with barium sulfate as a reference. The bandgap energies of the samples were determined from the absorption edge of the absorbance spectra represented by the Kubelka–Munk function, $f(R) = (1 - R)^2/2R$, where R is reflectance [46, 47]. The color properties of the samples were evaluated in terms of CIE $L^*a^*b^*CH°$ system with a chromometer (Konica-Minolta CR-300). In this system, the parameter L^* represents the brightness or darkness of a color relative to a neutral grey scale, while the parameters a^* (the red−green axis) and b^* (the yellow−blue axis) qualitatively express the color. The chroma parameter (C) represents the color saturation of pigments and is calculated according to the following formula: $C = [(a^*)^2 + (b^{*2})]^{½}$. The parameter $H°$ ranges from 0 to 360º, and is calculated with the formula, $H° = \tan^{-1}(b^* / a^*)$ (for pure red, $H° = 0$).

2.3 Results and Discussion

2.3.1 $Bi_4V_2O_{11}$

Figure 2.1 shows the XRD patterns of $Bi_4V_2O_{11}$ synthesized in a flow of air ($Bi_4V_2O_{11}$ (Air)) and pure O_2 ($Bi_4V_2O_{11}$ (O_2)). The orthorhombic $Bi_4V_2O_{11}$ structure was obtained in a single-phase form for both samples. **Table 2.1** lists the lattice volume of the samples calculated from the diffraction angle in the XRD patterns. The lattice volume of $Bi_4V_2O_{11}$ (O_2) was smaller than that of $Bi_4V_2O_{11}$ (Air). These results indicate that pentavalent Bi^{5+} ions were generated in the lattice of $Bi_4V_2O_{11}$ (O_2) by oxidization of trivalent Bi^{3+} ions, because the ionic radius of Bi^{5+} (0.076 nm) [44] is smaller than that of Bi^{3+} (0.103 nm) [44].

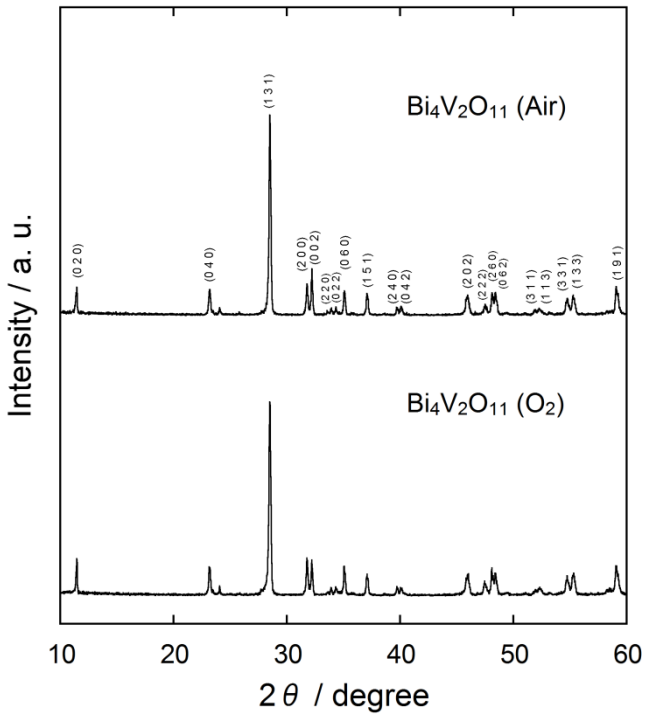

Figure 2.1 XRD patterns of the samples.

Table 2.1 Lattice volume of the samples

Samples	V / nm^3
$Bi_4V_2O_{11}$ (Air)	0.4729
$Bi_4V_2O_{11}$ (O_2)	0.4719

The valence states of the chemical species on near the surface for the $Bi_4V_2O_{11}$ (Air) and $Bi_4V_2O_{11}$ (O_2) samples were identified by XPS analysis without Ar etching. The XPS of the Bi 4f, V 2p, and O 1s core-levels for the samples were collected as illustrated in **Figure 2.2**. The peak shape and binding energies were obviously depended on the calcination atmosphere. In the case of the Bi 4f spectrum of $Bi_4V_2O_{11}$ (Air), the $4f_{5/2}$ and $4f_{7/2}$ peaks located at 164.1 eV and 158.8 eV can be assigned to those of trivalent Bi^{3+} [54, 55]. For $Bi_4V_2O_{11}$ (O_2), however, the additional shoulder peaks were observed at 165.8 eV and 160.5 eV corresponding to those of pentavalent Bi^{5+} [55].

On the other hand, in the cases of V 2p and O 1s for $Bi_4V_2O_{11}$ (Air), the $2p_{1/2}$ and $2p_{3/2}$ peaks located at 524.1 eV and 516.4 eV can be attributed to those of pentavalent V^{5+} [56], and 1s peak at 529.7 eV can be assigned to the lattice oxygen [56], respectively. In the spectrum of $Bi_4V_2O_{11}$ (O_2), however, some additional peaks appeared: a shoulder peak located at 531.3 eV can be attributed to an excess amount of oxygen species introduced into the lattice [56], and a shoulder peak located at 517.9 eV corresponding to V $2p_{3/2}$, which is considered to be attributable to the excessive oxygen species.

From the above results, it is revealed that partial oxidization of Bi^{3+} to Bi^{5+} occurred, due to the calcination of $Bi_4V_2O_{11}$ in a flow of pure O_2. As a result, oxide anions were introduced by the charge compensation mechanism into the blank oxide anion sites, which originally exists in the $Bi_4V_2O_{11}$ lattice. Accordingly, it is precise to express $Bi_4V_2O_{11}$ (O_2) and $Bi_4V_2O_{11}$ (Air) as $Bi_4V_2O_{11+\delta'}$ and $Bi_4V_2O_{11}$, respectively.

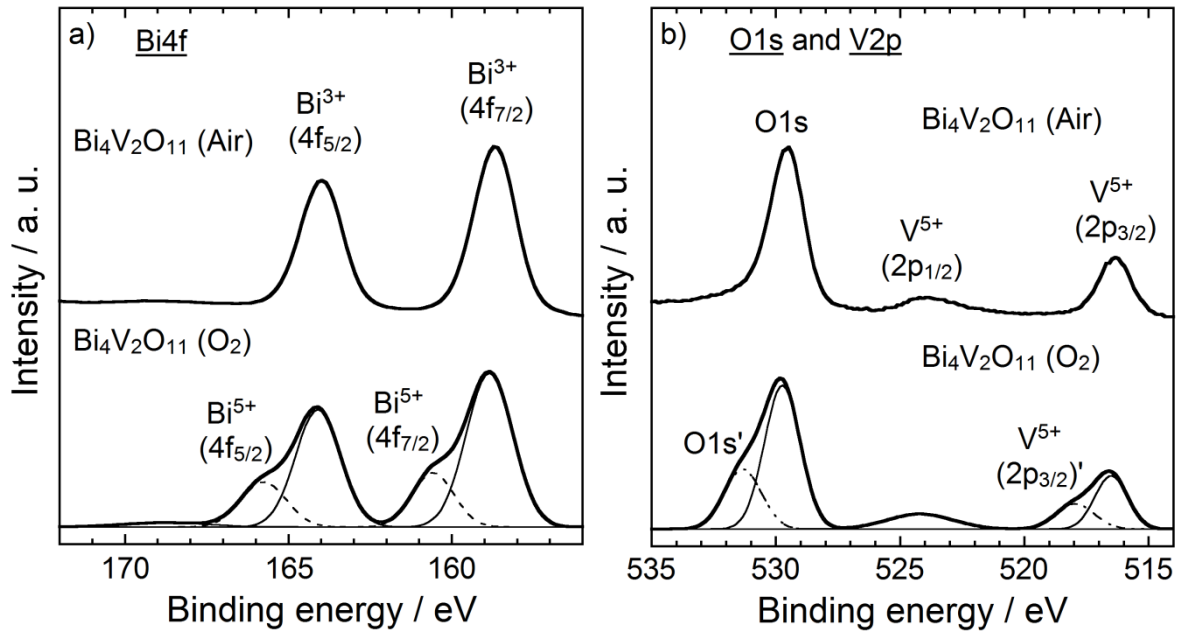

Figure 2.2 XPS of the Bi 4f (a), V 2p and O1s (b) core-levels for the samples.

Figure 2.3 depicts the UV-Vis diffuse reflectance spectra for $Bi_4V_2O_{11}$ and $Bi_4V_2O_{11+\delta'}$. In comparison to $Bi_4V_2O_{11}$, $Bi_4V_2O_{11+\delta'}$ reflected the red light (605 − 780 nm) more effectively. The CIE $L^*a^*b^*$ color coordinate data and bandgap energies (E_g) for the samples are summarized in **Table 2.2**. The a^* value, which corresponds to red component, for $Bi_4V_2O_{11+\delta'}$ (a^* = +37.1) was higher by about 10 points than that of $Bi_4V_2O_{11}$ (a^* = +27.3).

As already mentioned in the XPS analysis, pentavalent Bi^{5+} ions were partially generated in the $Bi_4V_2O_{11+\delta'}$ sample, and the amount of the blank oxide anion sites was decreased. Consequently, the impurity energy levels originated in these blank oxide anion sites in the band structure were partially eliminated from the $Bi_4V_2O_{11+\delta'}$ sample. Therefore, the reflection in the red light increased for $Bi_4V_2O_{11+\delta'}$, leading to the significant increase in the redness (a^*), although the bandgap energy of this sample was slightly larger than that of

$Bi_4V_2O_{11}$, as seen in **Table 2.2**. Based on these results, all pigments were synthesized in a flow of pure O_2 in the following sections.

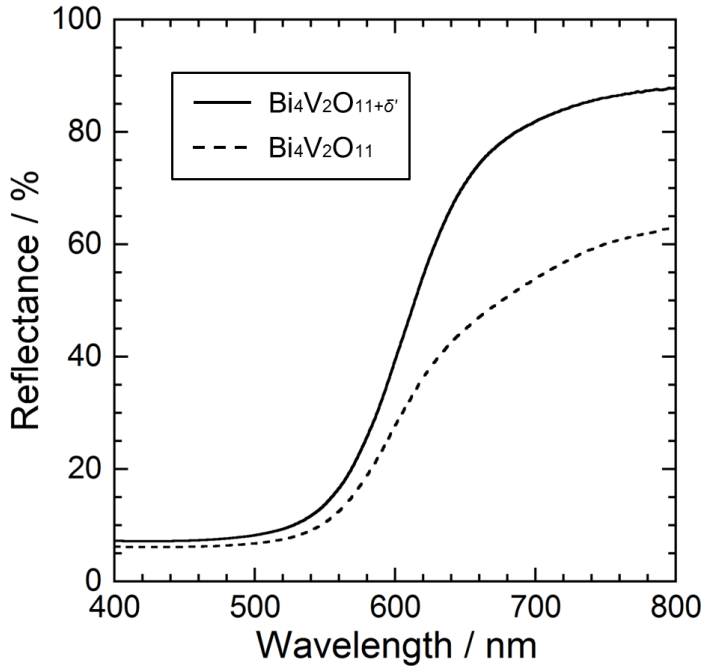

Figure 2.3 UV-Vis diffuse reflectance spectra for $Bi_4V_2O_{11}$ and $Bi_4V_2O_{11+\delta'}$.

Table 2.2 CIE $L^*a^*b^*$ color coordinate data and bandgap energies (E_g) for the samples

Samples	L^*	a^*	b^*	E_g / eV
$Bi_4V_2O_{11}$	43.5	+27.3	+29.3	2.15
$Bi_4V_2O_{11+\delta'}$	47.3	+37.1	+36.6	2.20

2.3.2 $(Bi_{1-x}Zr_x)_4V_2O_{11+\delta_I}$ $(0 \leq x \leq 0.15)$

Figure 2.4 shows the XRD patterns of the $(Bi_{1-x}Zr_x)_4V_2O_{11+\delta_I}$ $(0 \leq x \leq 0.15)$ samples. For $(Bi_{1-x}Zr_x)_4V_2O_{11+\delta_I}$ $(0 \leq x \leq 0.08)$, the orthorhombic $Bi_4V_2O_{11}$ structure was obtained in a single phase form, and no diffraction peaks of impurities were evident in the patterns. On the other hand, a monoclinic $BiVO_4$ structure was observed as an impurity phase in the patterns of $(Bi_{1-x}Zr_x)_4V_2O_{11+\delta_I}$ $(0.10 \leq x \leq 0.15)$, in addition to the main orthorhombic $Bi_4V_2O_{11}$ structure. The orthorhombic $Bi_4V_2O_{11}$ lattice volumes for the samples are listed in **Table 2.3**. The lattice volume linearly decreased with increasing Zr^{4+} content, in the single phase region $(0 \leq x \leq 0.08)$, because the ionic radius of Zr^{4+} (0.072 nm) [44] is smaller than those of Bi^{5+} (0.076 nm) [44] and Bi^{3+} (0.103 nm) [44] ions. However, the lattice volumes became approximately constant in the two-phase region $(0.10 \leq x \leq 0.15)$. These results indicate the formation of solid solutions with a single-phase orthorhombic $Bi_4V_2O_{11}$ structure, and the solubility limit of Zr^{4+} ions was about 8 mol% in $(Bi_{1-x}Zr_x)_4V_2O_{11+\delta_I}$.

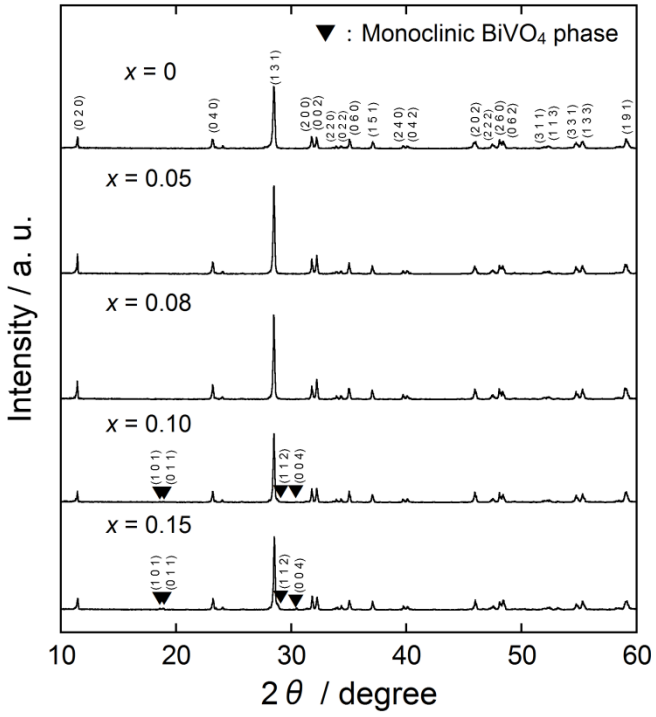

Figure 2.4 XRD patterns of the $(Bi_{1-x}Zr_x)_4V_2O_{11+\delta_I}$ $(0 \leq x \leq 0.15)$ samples.

Table 2.3 Lattice volume of the $(Bi_{1-x}Zr_x)_4V_2O_{11+\delta_l}$ $(0 \leq x \leq 0.15)$ samples

Samples	V / nm^3
$Bi_4V_2O_{11+\delta'}$	0.4719
$(Bi_{0.95}Zr_{0.05})_4V_2O_{11+\delta_{la}}$	0.4690
$(Bi_{0.92}Zr_{0.08})_4V_2O_{11+\delta_{lb}}$	0.4686
$(Bi_{0.90}Zr_{0.10})_4V_2O_{11+\delta_{lc}}$	0.4684
$(Bi_{0.85}Zr_{0.15})_4V_2O_{11+\delta_{ld}}$	0.4685

UV-Vis diffuse reflectance spectra for the $(Bi_{1-x}Zr_x)_4V_2O_{11+\delta_l}$ $(0 \leq x \leq 0.15)$ samples are depicted in **Figure 2.5**. In order to realize a red pigment, it is important to satisfy both high reflection in the red light region (605 − 780 nm) and effective absorption (*i.e.*, low reflection) in the green light region (490 − 560 nm), because green and red are the complementary colors. Strong reflection in the red light (605 − 780 nm) and effective absorption in the green light (490 − 560 nm) were observed for all samples. Therefore, these samples are red. Among the single-phase samples ($0 \leq x \leq 0.08$), the $(Bi_{0.92}Zr_{0.08})_4V_2O_{11+\delta_{lb}}$ sample reflects the red light most effectively. In the two-phase region ($0.10 \leq x \leq 0.15$), the absorption in the green light (490 − 560 nm) decreased, although further increase in the red light reflection was observed.

The CIE $L^*a^*b^*$ color coordinate data and bandgap energies (E_g) for the $(Bi_{1-x}Zr_x)_4V_2O_{11+\delta_l}$ $(0 \leq x \leq 0.15)$ samples are listed in **Table 2.4**. The a^* value, which corresponds to red chromaticity in the positive direction, increased with increasing the concentration of Zr^{4+} ions in the single phase region ($0 \leq x \leq 0.08$), and $(Bi_{0.92}Zr_{0.08})_4V_2O_{11+\delta_{lb}}$ exhibited the highest a^* value at +40.5. However, the redness (a^*) decreased in the two-phase samples ($0.10 \leq x \leq 0.15$), due to the formation of the impurity monoclinic $BiVO_4$ phase, which shows yellow hue as already described in **Chapter 1**.

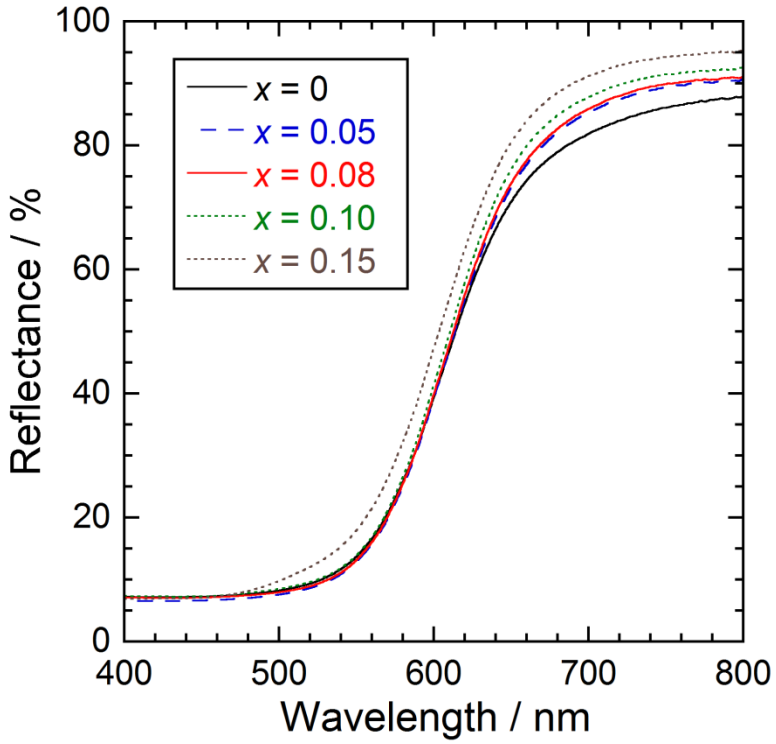

Figure 2.5 UV-Vis diffuse reflectance spectra of $(Bi_{1-x}Zr_x)_4V_2O_{11+\delta_l}$ $(0 \leq x \leq 0.15)$.

Table 2.4 CIE $L^*a^*b^*$ color coordinate data and bandgap energies (E_g) for the samples

Samples	L^*	a^*	b^*	E_g / eV
$Bi_4V_2O_{11+\delta'}$	47.3	+37.1	+36.6	2.20
$(Bi_{0.95}Zr_{0.05})_4V_2O_{11+\delta_{1a}}$	49.4	+39.7	+40.6	2.19
$(Bi_{0.92}Zr_{0.08})_4V_2O_{11+\delta_{1b}}$	49.6	+40.5	+41.1	2.18
$(Bi_{0.90}Zr_{0.10})_4V_2O_{11+\delta_{1c}}$	50.1	+40.4	+42.5	2.19
$(Bi_{0.85}Zr_{0.15})_4V_2O_{11+\delta_{1d}}$	52.1	+38.9	+44.5	2.33

2.3.3 $(Bi_{1-y}Al_y)_4V_2O_{11+\delta_3}$ $(0 \leq y \leq 0.10)$

Figure 2.6 depicts the XRD patterns of the $(Bi_{1-y}Al_y)_4V_2O_{11+\delta_3}$ $(0 \leq y \leq 0.10)$ samples. The orthorhombic $Bi_4V_2O_{11}$ phase was observed for the samples in which the Al^{3+} concentration was 5 mol% or less, and there were no diffraction peaks due to other impurities. In contrast, for the samples with the Al^{3+} content of more than 5 mol%, the monoclinic $BiVO_4$ structure was observed as a secondary phase. The orthorhombic $Bi_4V_2O_{11}$ lattice volumes for the $(Bi_{1-y}Al_y)_4V_2O_{11+\delta_3}$ $(0 \leq y \leq 0.10)$ samples are tabulated in **Table 2.5**. The lattice volume proportionally decreased with increasing the amount of Al^{3+} in the single-phase region $(0 \leq y \leq 0.05)$, because the ionic radius of Al^{3+} (0.0535 nm) [44] is smaller than those of Bi^{5+} (0.076 nm) [44] and Bi^{3+} (0.103 nm) [44]. However, the lattice volume became nearly constant in the two-phase region $(0.05 < y \leq 0.10)$. From these results, it is suggested that solid solutions of the orthorhombic $Bi_4V_2O_{11}$ structure were formed successfully for $(Bi_{1-y}Al_y)_4V_2O_{11+\delta_3}$ $(0 < y \leq 0.05)$, and the solubility limit of Al^{3+} ions was around 5 mol% in $(Bi_{1-y}Al_y)_4V_2O_{11+\delta_3}$.

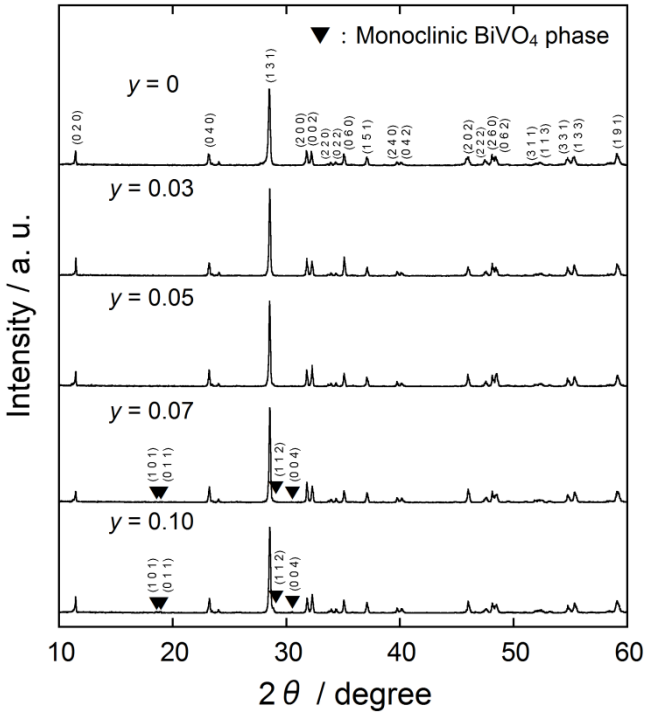

Figure 2.6 XRD patterns of the $(Bi_{1-y}Al_y)_4V_2O_{11+\delta_3}$ $(0 \leq y \leq 0.10)$ samples.

Table 2.5 Lattice volumes for the $(Bi_{1-y}Al_y)_4V_2O_{11+\delta_3}$ $(0 \le y \le 0.10)$ samples

Samples	V / nm^3
$Bi_4V_2O_{11+\delta'}$	0.4719
$(Bi_{0.97}Al_{0.03})_4V_2O_{11+\delta_{3a}}$	0.4681
$(Bi_{0.95}Al_{0.05})_4V_2O_{11+\delta_{3b}}$	0.4678
$(Bi_{0.93}Al_{0.07})_4V_2O_{11+\delta_{3c}}$	0.4679
$(Bi_{0.90}Al_{0.10})_4V_2O_{11+\delta_{3d}}$	0.4677

Figure 2.7 illustrates the UV-Vis diffuse reflectance spectra of the $(Bi_{1-y}Al_y)_4V_2O_{11+\delta_3}$ $(0 \le y \le 0.10)$ samples. For $(Bi_{1-y}Al_y)_4V_2O_{11+\delta_3}$ $(0 \le y \le 0.05)$, which were obtained in the single orthorhombic $Bi_4V_2O_{11}$ phase, the absorption in the green light region (490 − 560 nm) increased with increasing the amount of Al^{3+}. Among them, $(Bi_{0.97}Al_{0.03})_4V_2O_{11+\delta_{3a}}$ reflected the red light (605 − 780 nm) most effectively, although the green light (490 − 560 nm) absorption of this sample was weaker than that of $(Bi_{0.95}Al_{0.05})_4V_2O_{11+\delta_{3b}}$.

Table 2.6 lists the CIE $L^*a^*b^*$ color coordinate data and bandgap energies (E_g) for the $(Bi_{1-y}Al_y)_4V_2O_{11+\delta_3}$ $(0 \le y \le 0.10)$ samples. The a^* value representing the red chromaticity of the pigments depended on their compositions, and the most highest redness was obtained for $(Bi_{0.97}Al_{0.03})_4V_2O_{11+\delta_{3a}}$ (a^* = +41.6), as in the UV-Vis diffuse reflectance measurement.

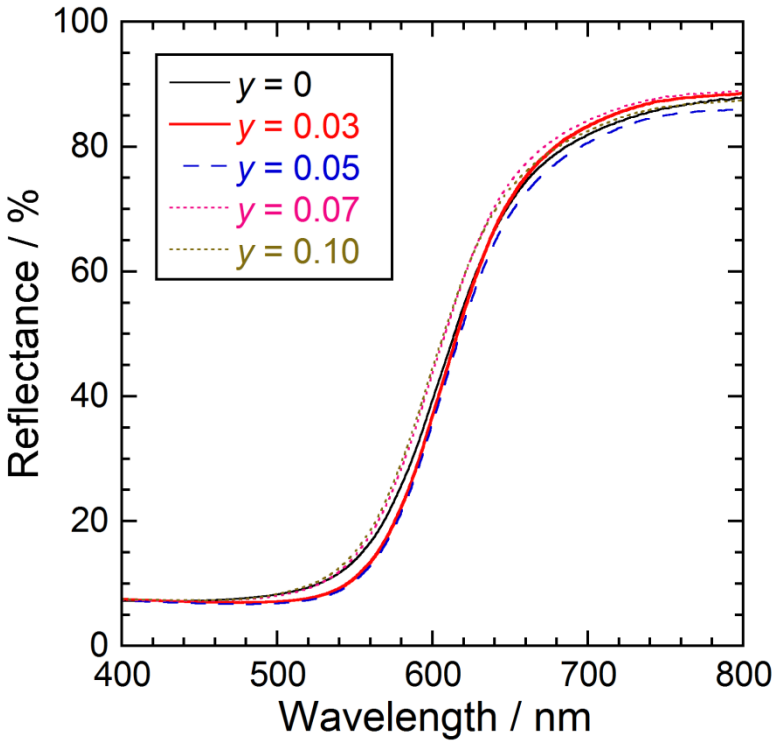

Figure 2.7 UV-Vis diffuse reflectance spectra of the $(Bi_{1-y}Al_y)_4V_2O_{11+\delta_3}$ ($0 \leq y \leq 0.10$) samples.

Table 2.6 CIE $L^*a^*b^*$ color coordinate data and bandgap energies (E_g) for the samples

Samples	L^*	a^*	b^*	E_g / eV
$Bi_4V_2O_{11+\delta'}$	47.3	+37.1	+36.6	2.20
$(Bi_{0.97}Al_{0.03})_4V_2O_{11+\delta_{3a}}$	47.7	+41.6	+38.0	2.17
$(Bi_{0.95}Al_{0.05})_4V_2O_{11+\delta_{3b}}$	47.8	+40.6	+36.8	2.19
$(Bi_{0.93}Al_{0.07})_4V_2O_{11+\delta_{3c}}$	52.5	+40.2	+38.8	2.20
$(Bi_{0.90}Al_{0.10})_4V_2O_{11+\delta_{3d}}$	53.0	+36.9	+43.4	2.21

2.3.4 $(Bi_{1-x-y}Zr_xAl_y)_4V_2O_{11+\delta_2}$ $(0.01 \leq x \leq 0.07;\ 0.01 \leq y \leq 0.07)$

As mentioned in the previous sections, dissolution of Zr^{4+} or Al^{3+} into the $Bi_4V_2O_{11+\delta'}$ lattice is effective to increase the red hue of the obtained pigments. In this section, therefore, both Zr^{4+} and Al^{3+} were doped into the $Bi_4V_2O_{11+\delta'}$ lattice and the composition was optimized to produce the most vivid red color. In this regard, the total amount of Zr^{4+} and Al^{3+} was kept constant at 8 mol%, because an excess amount of the dopants had opposite effect on the red hue of the pigments by the formation of yellowish monoclinic $BiVO_4$ phase as an impurity.

XRD patterns of the $(Bi_{1-x-y}Zr_xAl_y)_4V_2O_{11+\delta_2}$ $(0.01 \leq x \leq 0.07;\ 0.01 \leq y \leq 0.07)$ samples are presented in **Figure 2.8**. The orthorhombic $Bi_4V_2O_{11}$ structure was obtained in a single-phase form for all samples. As shown in **Table 2.7**, the lattice volumes of the $(Bi_{1-x-y}Zr_xAl_y)_4V_2O_{11+\delta_2}$ $(0.01 \leq x \leq 0.07;\ 0.01 \leq y \leq 0.07)$ samples were smaller than that of the non-doped $Bi_4V_2O_{11+\delta'}$ sample, indicating that the formation of solid solutions.

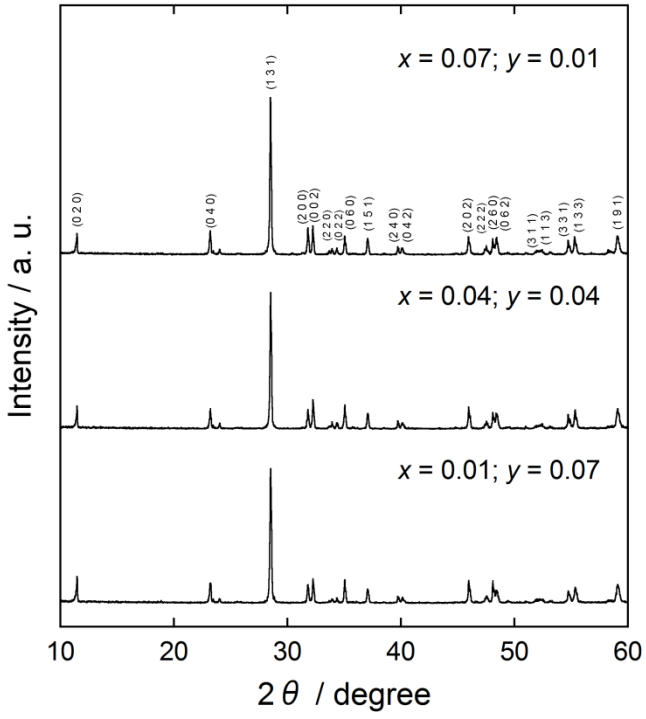

Figure 2.8 XRD patterns of the $(Bi_{1-x-y}Zr_xAl_y)_4V_2O_{11+\delta_2}$ $(0.01 \leq x \leq 0.07;\ 0.01 \leq y \leq 0.07)$ samples.

Table 2.7 Lattice volume of the samples

Samples	V / nm^3
$Bi_4V_2O_{11+\delta'}$	0.4719
$(Bi_{0.92}Zr_{0.07}Al_{0.01})_4V_2O_{11+\delta_{2a}}$	0.4684
$(Bi_{0.92}Zr_{0.04}Al_{0.04})_4V_2O_{11+\delta_{2b}}$	0.4681
$(Bi_{0.92}Zr_{0.01}Al_{0.07})_4V_2O_{11+\delta_{2c}}$	0.4678

Figure 2.9 depicts the UV-Vis diffuse reflectance spectra for the $(Bi_{1-x-y}Zr_xAl_y)_4V_2O_{11+\delta_2}$ ($0.01 \le x \le 0.07$; $0.01 \le y \le 0.07$) samples. Both the reflection in the red light (605 − 780 nm) and the absorption in the green light (490 − 560 nm) were dependent on their compositions. Among these pigments, the $(Bi_{0.92}Zr_{0.07}Al_{0.01})_4V_2O_{11+\delta_{2a}}$ pigment presented the most effective reflection in the red light region (605 − 780 nm).

In **Table 2.8**, CIE $L^*a^*b^*CH^o$ color coordinate data and bandgap energies (E_g) for the $(Bi_{1-x-y}Zr_xAl_y)_4V_2O_{11+\delta_2}$ ($0.01 \le x \le 0.07$; $0.01 \le y \le 0.07$) samples are summarized. The a^* value corresponding to the red chromaticity depended on their compositions, and the highest red hue was obtained for $(Bi_{0.92}Zr_{0.07}Al_{0.01})_4V_2O_{11+\delta_{2a}}$ and $(Bi_{0.92}Zr_{0.04}Al_{0.04})_4V_2O_{11+\delta_{2b}}$, where $a^* = +41.9$ for both samples. Furthermore, the hue angle (H^o), which corresponds to color purity, for $(Bi_{0.92}Zr_{0.07}Al_{0.01})_4V_2O_{11+\delta_{2a}}$ ($H^o = 39.0$) was smaller than that for $(Bi_{0.92}Zr_{0.04}Al_{0.04})_4V_2O_{11+\delta_{2b}}$ ($H^o = 40.0$). Therefore, $(Bi_{0.92}Zr_{0.07}Al_{0.01})_4V_2O_{11+\delta_{2a}}$ produced the deepest red hue among these pigments.

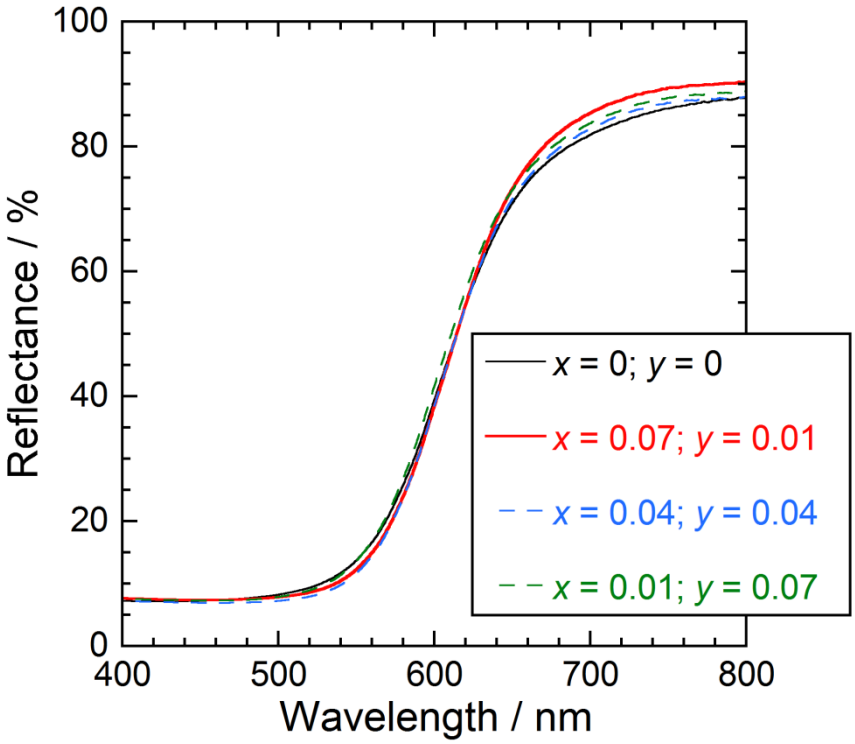

Figure 2.9 UV-Vis diffuse reflectance spectra for the $(Bi_{1-x-y}Zr_xAl_y)_4V_2O_{11+\delta_2}$ ($0.01 \leq x \leq 0.07$; $0.01 \leq y \leq 0.07$) samples.

Table 2.8 CIE $L^*a^*b^*CH^o$ color coordinate data and bandgap energies (E_g) for the samples

Samples	L^*	a^*	b^*	C	H^o	E_g / eV
$Bi_4V_2O_{11+\delta'}$	47.3	+37.1	+36.6	52.1	44.6	2.20
$(Bi_{0.92}Zr_{0.07}Al_{0.01})_4V_2O_{11+\delta_{2a}}$	49.6	+41.9	+34.0	53.9	39.0	2.18
$(Bi_{0.92}Zr_{0.04}Al_{0.04})_4V_2O_{11+\delta_{2b}}$	49.7	+41.9	+35.2	54.7	40.0	2.18
$(Bi_{0.92}Zr_{0.01}Al_{0.07})_4V_2O_{11+\delta_{2c}}$	51.2	+38.9	+43.2	58.1	48.0	2.19

Bi L_{III} XANES spectra of non-doped $Bi_4V_2O_{11+\delta'}$, $(Bi_{0.92}Zr_{0.08})_4V_2O_{11+\delta_{1b}}$, and $(Bi_{0.97}Al_{0.03})_4V_2O_{11+\delta_{3a}}$ are shown in **Figure 2.10**, with that of α-Bi_2O_3 as the standard of Bi^{3+}. In the spectra of non-doped $Bi_4V_2O_{11+\delta'}$, $(Bi_{0.92}Zr_{0.08})_4V_2O_{11+\delta_{1b}}$, and $(Bi_{0.97}Al_{0.03})_4V_2O_{11+\delta_{3a}}$, a peak assigned to pentavalent Bi^{5+} ions was observed at 13,440 eV [57]. On the contrary, this peak was absent in the spectrum of α-Bi_2O_3, in which bismuth ions exist only in trivalent state. In addition, the absorption edge shift to the higher energy side was observed for these pigments, compared with that of α-Bi_2O_3. These results elucidate the existence of pentavalent Bi^{5+} ions in the bulk of the non-doped $Bi_4V_2O_{11+\delta'}$, $(Bi_{0.92}Zr_{0.08})_4V_2O_{11+\delta_{1b}}$, and $(Bi_{0.97}Al_{0.03})_4V_2O_{11+\delta_{3a}}$ pigments.

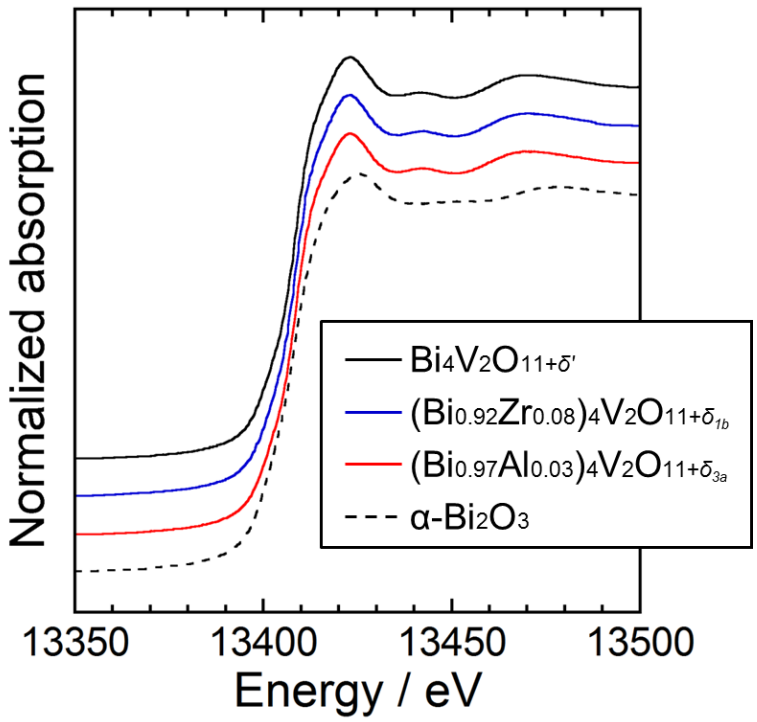

Figure 2.10 Bi L_{III} XANES spectra of $Bi_4V_2O_{11+\delta'}$, $(Bi_{0.92}Zr_{0.08})_4V_2O_{11+\delta_{1b}}$, and $(Bi_{0.97}Al_{0.03})_4V_2O_{11+\delta_{3a}}$ and α-Bi_2O_3.

Figure 2.11 illustrates XPS of $(Bi_{0.92}Zr_{0.08})_4V_2O_{11+\delta_{1b}}$, $(Bi_{0.97}Al_{0.03})_4V_2O_{11+\delta_{3a}}$, and $(Bi_{0.92}Zr_{0.07}Al_{0.01})_4V_2O_{11+\delta_{2a}}$. The spectrum of non-doped $Bi_4V_2O_{11+\delta'}$ is also depicted for comparison. The proportion of pentavalent Bi^{5+} in total bismuth ions (Bi^{5+} / (Bi^{5+}+Bi^{3+})) for these pigments was estimated from the peak area in the spectra, and the results are listed in **Table 2.9**. The proportion of Bi^{5+} was 35 % for $(Bi_{0.92}Zr_{0.08})_4V_2O_{11+\delta_{1b}}$, while it was 26 % for non-doped $Bi_4V_2O_{11+\delta'}$. These results suggest that the amount of Bi^{5+} was increased by the Zr^{4+} doping into the bismuth sites of the $Bi_4V_2O_{11+\delta'}$ lattice, and thereby, the blank oxide anion sites were decreased in $(Bi_{0.92}Zr_{0.08})_4V_2O_{11+\delta_{1b}}$, because of the reason already mentioned in **Section 2.3.1**.

In the case of $(Bi_{0.97}Al_{0.03})_4V_2O_{11+\delta_{3a}}$, the proportion of Bi^{5+} for this pigment (21 %) was lower than that for non-doped $Bi_4V_2O_{11+\delta'}$ (26 %). The binding energies of $Bi4f_{7/2}$ (159.6 eV) and $Bi4f_{5/2}$ (164.9 eV) attributable to those of pentavalent Bi^{5+} were observed at lower energies than those of non-doped $Bi_4V_2O_{11+\delta'}$: $Bi4f_{7/2}$ (160.5 eV) and $Bi4f_{5/2}$ (165.8 eV). These results indicate that significant lattice shrinkage was occurred in the $(Bi_{0.97}Al_{0.03})_4V_2O_{11+\delta_{3a}}$ lattice to induce significant electronic repulsion in the 4f orbital, even the 4f electrons are well shielded from the surroundings by the 5d and 6s orbitals. As a result, the conduction band composed of the V_{3d} orbital was also enlarged by the lattice shrinking to increase the crystal field splitting. In fact, the bandgap energy for this pigment was the smallest among the three samples. Furthermore, in the case of the $(Bi_{0.92}Zr_{0.07}Al_{0.01})_4V_2O_{11+\delta_{2a}}$ pigment, both of the increase in the proportion of Bi^{5+} and the decrease in the binding energies of $Bi4f_{7/2}$ and $Bi4f_{5/2}$ were confirmed.

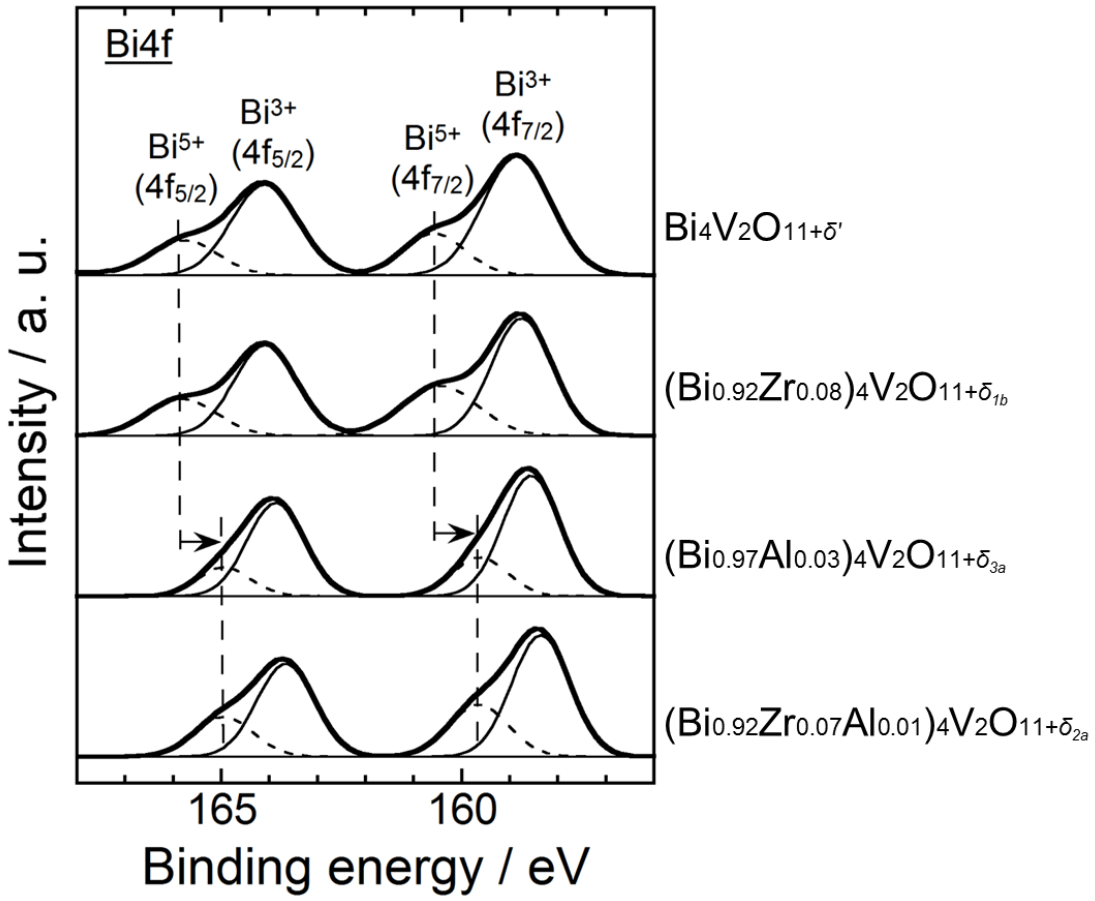

Figure 2.11 XPS of the $Bi_4V_2O_{11+\delta'}$, $(Bi_{0.92}Zr_{0.08})_4V_2O_{11+\delta_{1b}}$, $(Bi_{0.97}Al_{0.03})_4V_2O_{11+\delta_{3a}}$, and $(Bi_{0.92}Zr_{0.07}Al_{0.01})_4V_2O_{11+\delta_{2a}}$ samples.

Table 2.9 The proportion of pentavalent Bi^{5+} (Bi^{5+} / (Bi^{5+}+Bi^{3+})) for the samples

Samples	Proportion of Bi^{5+} / %
$Bi_4V_2O_{11+\delta'}$	26
$(Bi_{0.92}Zr_{0.08})_4V_2O_{11+\delta_{1b}}$	35
$(Bi_{0.97}Al_{0.03})_4V_2O_{11+\delta_{3a}}$	21
$(Bi_{0.92}Zr_{0.07}Al_{0.01})_4V_2O_{11+\delta_{2a}}$	30

Taking into account of these results, the doping effect of Zr^{4+} and Al^{3+} on the red hue of the pigments can be summarized as follows.

Doping effect of Zr^{4+}: The Zr^{4+} doping into the bismuth sites in the $Bi_4V_2O_{11+\delta'}$ lattice positively affects the color property: the blank oxide anion sites were occupied by the charge compensation mechanism, leading to the elimination of the impurity energy levels between the valence and the conduction bands in the band structure. However, the introduction of an excess amount of Zr^{4+} ions induces the formation of yellowish monoclinic $BiVO_4$ as an impurity phase to decrease the redness value.

Doping effect of Al^{3+}: Dissolution of Al^{3+} reduces the bandgap energy of the $Bi_4V_2O_{11+\delta'}$ by broadening the width of V_{3d} valence band, although it increases the amount of the blank oxide anion sites (oxide anion vacancies). Accordingly, both positive and negative effects are produced simultaneously. It is considered that the positive effect is dominant when a small amount of Al^{3+} is doped into the lattice, but adversely the negative effect will become prominent when the amount of Al^{3+} is large.

Consequently, the synergetic effects of both mentioned above was observed when both Zr^{4+} and Al^{3+} were doped into the $Bi_4V_2O_{11+\delta'}$ lattice. As a result, the band structure was optimized for the $(Bi_{0.92}Zr_{0.07}Al_{0.01})_4V_2O_{11+\delta_{2a}}$ pigment.

Table 2.10 lists the CIE $L^*a^*b^*CH^o$ color coordinate data and bandgap energies (E_g) of the $(Bi_{0.92}Zr_{0.07}Al_{0.01})_4V_2O_{11+\delta_{2a}}$ pigment, the commercial cadmium selenide red (Holbein works, Ltd., PG002), commercial mercuric sulfide red (Holbein works, Ltd., PG009), and commercial iron oxide (Morishita Bengara Kogyo Co. Ltd., MR-320A) pigments. Although the redness value and the color saturation parameter for the $(Bi_{0.92}Zr_{0.07}Al_{0.01})_4V_2O_{11+\delta_{2a}}$ pigment (a^* = +41.9, C = 53.9) fell short of those for the toxic cadmium selenide red (a^* = +63.7, C = 84.6) and mercuric sulfide red (a^* = +56.5, C = 69.5) pigments, they are significantly greater than those for the environmentally friendly iron oxide pigment (a^* =

+28.9, C = 38.4). In addition, the brightness value of this pigment (L^* = 49.6) was also larger than that of the iron oxide pigment (L^* = 38.9), indicating that the $(Bi_{0.92}Zr_{0.07}Al_{0.01})_4V_2O_{11+\delta_{2a}}$ pigment produced a light red hue.

Table 2.10 CIE $L^*a^*b^*CH^o$ color coordinate data and bandgap energies (E_g) of the pigments

Pigments	L^*	a^*	b^*	C	H^o	E_g / eV
$(Bi_{0.92}Zr_{0.07}Al_{0.01})_4V_2O_{11+\delta_{2a}}$	49.6	+41.9	+34.0	53.9	39.0	2.18
Commercial cadmium selenide red (CdS-CdSe)	51.9	+63.7	+55.8	84.6	41.2	2.11
Commercial mercuric sulfide red (HgS)	52.0	+56.5	+40.5	69.5	35.6	2.13
Commercial iron oxide (Fe_2O_3)	38.9	+28.9	+25.3	38.4	41.2	2.21

2.4 Conclusion

Novel environmentally friendly red pigments, $(Bi_{1-x-y}Zr_xAl_y)_4V_2O_{11+\delta}$ ($0 \le x \le 0.15$; $0 \le y \le 0.10$), were successfully synthesized by a conventional solid state reaction method. The color of the pigments depended on the calcination condition and the composition, and the most vivid red hue was obtained for $(Bi_{0.92}Zr_{0.07}Al_{0.01})_4V_2O_{11+\delta_{2a}}$, which has CIE $L^*a^*b^*$ color parameters of L^* = 49.6, a^* = +41.9, and b^* = +34.0. The a^* value corresponds to the redness was significantly higher than that of a commercially available iron oxide pigment (a^* = +28.9). Since $Bi_4V_2O_{11}$ is considered to be a nontoxic compound, and Zr and Al are also nontoxic and safe elements, the present pigments should be effective alternatives for the conventional iron oxide pigment.

Chapter 3

Synthesis of Novel Inorganic Blue Pigments Based on Calcium Scandium Silicate Garnet ($Ca_3Sc_2Si_3O_{12}$)

3.1 Introduction

In this chapter, novel environmentally friendly inorganic blue pigments are described. Initially, tungsten oxyphosphate (WOP_2O_7) was focused on as an attractive candidate. This compound is composed of only nontoxic and safe elements (W, P, and O) and the color is dark blue when it is amorphous [58]. The color of amorphous WOP_2O_7 depends on the amount of W^{5+} in this compound, and can be tuned by doping rare earth ions to control the W^{5+} concentration. In fact, amorphous $(W_{1-x}Ln_x)OP_2O_{7-\delta}$ ($0.10 \leq x \leq 0.29$; Ln = La, Eu, Gd, Y, and Lu) materials were successfully synthesized and these pigments showed brilliant blue colors in comparison with that of amorphous WOP_2O_7. Unfortunately, however, thermal stability of these pigments was insufficient, because they are amorphous.

Because of this situation, our research group focused on calcium scandium silicate ($Ca_3Sc_2Si_3O_{12}$), because this compound adopts a thermally and chemically stable garnet-type structure and is composed of only nontoxic elements (Ca, Sc, Si, and O). However, $Ca_3Sc_2Si_3O_{12}$ is white, but in this study, it has been found that a surprisingly intense bright-blue color is obtained when divalent Eu^{2+} ions are introduced into the Ca^{2+} sites in the $Ca_3Sc_2Si_3O_{12}$ lattice. These materials are expected to be environmentally friendly inorganic blue pigments, because europium is also a nontoxic and safe element. Therefore, $(Ca_{1-x}Eu_x)_3Sc_2Si_3O_{12+\delta}$ ($0 \leq x \leq 0.10$) samples were synthesized, and the compositions and the preparation conditions were optimized to produce the most vivid blue hue.

3.2 Experimental Procedure

The $(Ca_{1-x}Eu_x)_3Sc_2Si_3O_{12+\delta}$ ($0 \leq x \leq 0.10$) pigments were synthesized by a conventional solid state reaction method. $CaCO_3$, Eu_2O_3, Sc_2O_3, and SiO_2 powders were mixed in a stoichiometric ratio in an agate mortar. Then, the mixture was mechanically mixed using a planetary-type ball-milling apparatus (PULVERISETTE 7 premium line, Fritsch GmbH) for 3 h. The homogenous mixture was calcined at 1300, 1350, 1375, or 1400 ºC for 4, 6, or 8 h in a flow of 2%H_2−98%Ar gas for the reduction of Eu^{3+} to Eu^{2+}. In some cases, the pigment was washed with a dilute hydrochloric acid solution (2%), where the sample (0.1 g) was soaked into 15 cm^3 of the HCl solution and the suspension was stirred for 10 min at room temperature. The pigment was collected by filtration, washed with deionized water and ethanol until the pH of the supernatant solution becomes neutral. Finally, the pigment was dried at 80 ºC for 3 h. Before characterization, the samples were gently ground in an agate mortar.

The samples were characterized by X-ray powder diffraction (XRD; Rigaku SmartLab) using Cu-Kα radiation (40 kV, 30 mA) to identify their crystal structure. The compositions of the samples were analyzed by X-ray fluorescence spectroscopy (XRF; Rigaku ZSX-100e). The optical reflectance spectra were obtained using a UV-Vis spectrometer (Shimadzu UV-2600) with barium sulfate as a reference. The spectra of all samples were measured in a green pellet form (0.3 g) without any additives. The color properties of the samples were estimated in terms of the CIE $L^*a^*b^*$ system with a colorimeter (Konica-Minolta CR-300). The parameter L^* represents the brightness or darkness of a color relative to a neutral grey scale, while the parameters a^* (the red−green axis) and b^* (the yellow−blue axis) express the color qualitatively.

3.3 Results and Discussion

The compositions of all samples were confirmed by the XRF analysis to be in good agreement with their stoichiometric values. **Figure 3.1** depicts the XRD patterns of the $(Ca_{1-x}Eu_x)_3Sc_2Si_3O_{12+\delta}$ ($0 \leq x \leq 0.10$) samples calcined at 1350 ºC for 4 h. For all samples, the garnet-type $Ca_3Sc_2Si_3O_{12}$ phase was obtained almost in a single phase form, although a nominal amount of SiO_2 and Sc_2O_3 were observed as impurity phases. It is difficult to confirm the formation of solid solutions, because there was no peak shift in the XRD patterns with increasing europium content. The ionic radius of Eu^{3+} (0.1066 nm) [44] is smaller than that of Ca^{2+} (0.112 nm) [44], but that of Eu^{2+} (0.125 nm) [44] is larger. Therefore, it is suggested that europium ions in the $Ca_3Sc_2Si_3O_{12}$ lattice exist both in trivalent and divalent states. From their ionic sizes, the relative ratio of Eu^{3+}:Eu^{2+} was estimated to be approximately 71:29.

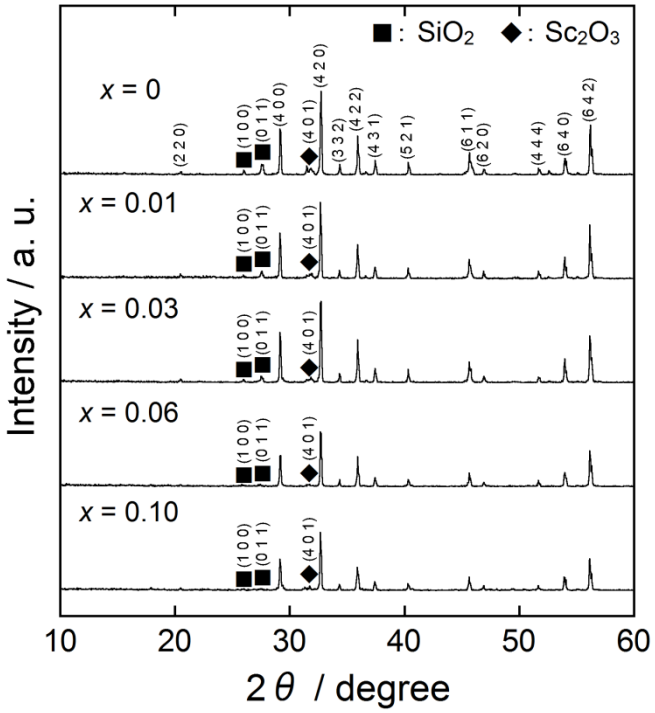

Figure 3.1 XRD patterns of the $(Ca_{1-x}Eu_x)_3Sc_2Si_3O_{12+\delta}$ ($0 \leq x \leq 0.10$) samples calcined at 1350 ºC for 4 h.

Figure 3.2 illustrates UV-Vis diffuse reflectance spectra for the $(Ca_{1-x}Eu_x)_3Sc_2Si_3O_{12+\delta}$ ($0 \leq x \leq 0.10$) samples calcined at 1350 ºC for 4 h. High reflection was observed throughout the visible light region for non-doped $Ca_3Sc_2Si_3O_{12}$ sample, because it is white. On the other hand, for the $(Ca_{1-x}Eu_x)_3Sc_2Si_3O_{12+\delta}$ ($0.01 \leq x \leq 0.10$) samples, strong reflection peaks were confirmed only at wavelengths between 430 and 500 nm including the blue region (435 − 480 nm), and therefore, these samples are blue. The blueness of the pigment is also affected by the optical reflection or absorption in the yellow region (570 − 590 nm), because yellow is the complementary color of blue. To realize brilliant blue color, it is important to satisfy both high reflection of blue light and effective absorption (*i.e.*, low reflection) of yellow light in **Figure 3.2**. Among these samples, a $(Ca_{0.94}Eu_{0.06})_3Sc_2Si_3O_{12+\delta}$ pigment exhibited moderate reflection in the blue light region (435 − 480 nm) and the most effective absorption in the yellow light region (570 − 590 nm).

The CIE $L^*a^*b^*$ color coordinate data for the $(Ca_{1-x}Eu_x)_3Sc_2Si_3O_{12+\delta}$ ($0 \leq x \leq 0.10$) samples are summarized in **Table 3.1**. For non-doped $Ca_3Sc_2Si_3O_{12}$, the brightness parameter L^* was large (93.3), but the chromaticity parameters a^* and b^* were around 0. However, these parameters varied significantly with the introduction of europium ions into the $Ca_3Sc_2Si_3O_{12}$ lattice. In particular, the b^* value, which corresponds to the blue chromaticity in the negative direction, decreased with increasing the europium concentration, and $(Ca_{0.94}Eu_{0.06})_3Sc_2Si_3O_{12+\delta}$ has the lowest b^* value (−30.1). Consequently, the $(Ca_{0.94}Eu_{0.06})_3Sc_2Si_3O_{12+\delta}$ pigment shows the most bluish hue among the $(Ca_{1-x}Eu_x)_3Sc_2Si_3O_{12+\delta}$ samples.

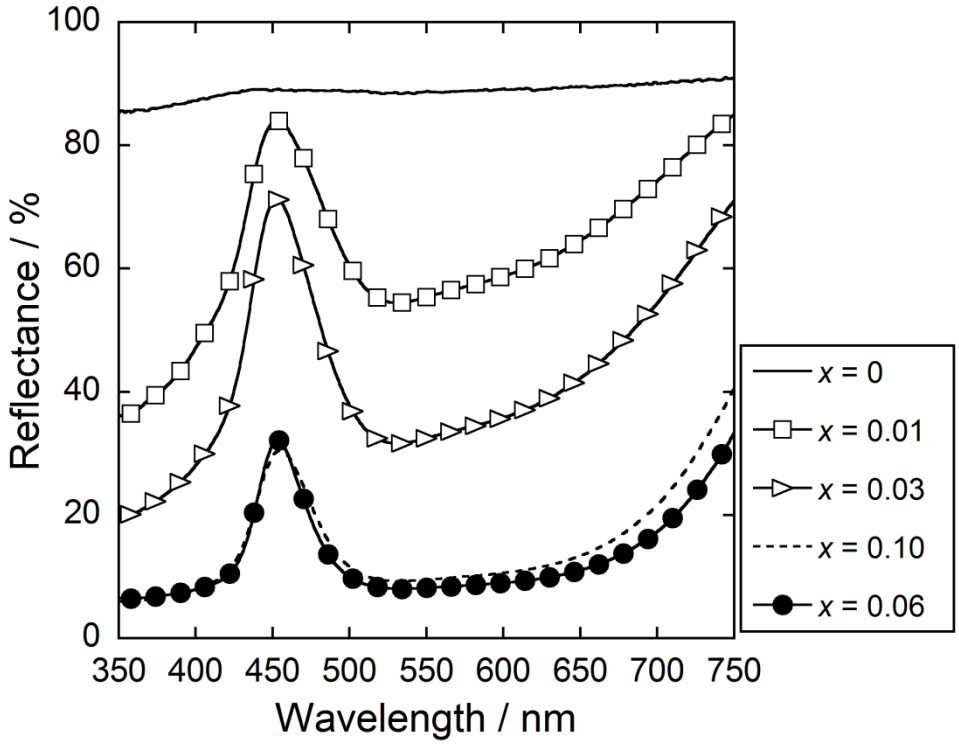

Figure 3.2 UV-Vis diffuse reflectance spectra for the $(Ca_{1-x}Eu_x)_3Sc_2Si_3O_{12+\delta}$ ($0 \leq x \leq 0.10$) samples calcined at 1350 ºC for 4 h.

Table 3.1 CIE $L^*a^*b^*$ color coordinate data for the $(Ca_{1-x}Eu_x)_3Sc_2Si_3O_{12+\delta}$ ($0 \leq x \leq 0.10$) samples calcined at 1350 ºC for 4 h

Pigments	L^*	a^*	b^*
$Ca_3Sc_2Si_3O_{12}$	93.3	+1.61	+0.19
$(Ca_{0.99}Eu_{0.01})_3Sc_2Si_3O_{12+\delta}$	78.7	+11.1	−14.0
$(Ca_{0.97}Eu_{0.03})_3Sc_2Si_3O_{12+\delta}$	66.4	+16.9	−22.7
$(Ca_{0.94}Eu_{0.06})_3Sc_2Si_3O_{12+\delta}$	36.8	+22.9	−30.1
$(Ca_{0.90}Eu_{0.10})_3Sc_2Si_3O_{12+\delta}$	40.1	+19.1	−25.6

As mentioned above, it is evident that dissolution of europium ions into the $Ca_3Sc_2Si_3O_{12}$ lattice is effective in increasing the blueness of the sample, and the optimum amount of Eu was 6 mol% to produce the most vivid blue hue. However, calcination temperature and period are also important factors which affect the color of resulting materials, because solid state reactions are dependent on these reaction conditions. Therefore, the synthesis condition for the $(Ca_{0.94}Eu_{0.06})_3Sc_2Si_3O_{12+\delta}$ pigment was optimized to further improve its blueness value.

First, the $(Ca_{0.94}Eu_{0.06})_3Sc_2Si_3O_{12+\delta}$ samples were synthesized at various temperatures, where the calcination time was fixed at 4 h. XRD patterns of the $(Ca_{0.94}Eu_{0.06})_3Sc_2Si_3O_{12+\delta}$ samples calcined at 1300, 1350, 1375, and 1400 ºC for 4 h are shown in **Figure 3.3**. The garnet-type $Ca_3Sc_2Si_3O_{12}$ phase was obtained almost in a single phase form for all samples.

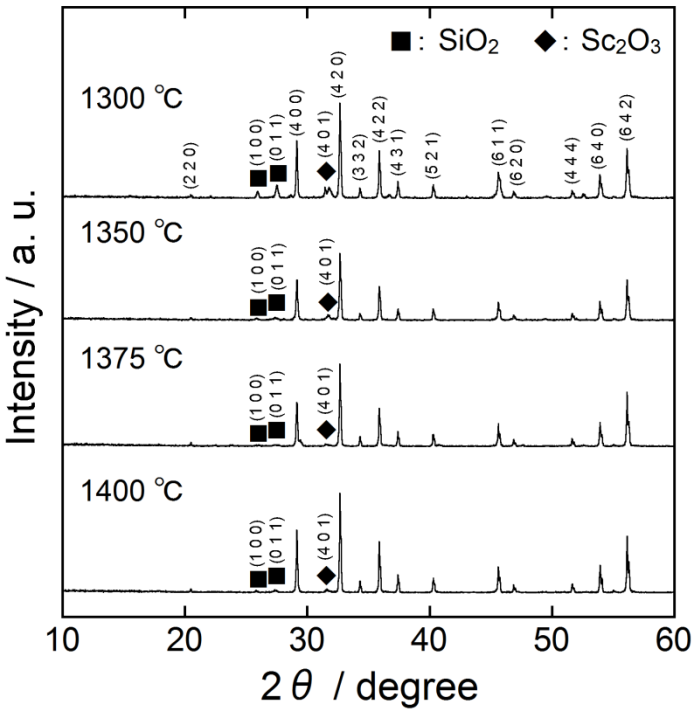

Figure 3.3 XRD patterns of the $(Ca_{0.94}Eu_{0.06})_3Sc_2Si_3O_{12+\delta}$ samples synthesized at 1300, 1350, 1375, and 1400 ºC for 4 h.

Nominal amounts of SiO_2 and Sc_2O_3 phases were still observed as impurities even after the calcination at 1400 ºC, although the peak intensities corresponding to these impurity phases decreased with increasing the temperature.

Figure 3.4 shows the UV-Vis diffuse reflectance spectra for the $(Ca_{0.94}Eu_{0.06})_3Sc_2Si_3O_{12+\delta}$ samples synthesized at different temperatures. Except for the sample synthesized at 1300 ºC, similar results were obtained: moderate reflection peaks were observed in the blue region (435 − 480 nm).

The CIE $L^*a^*b^*$ color coordinate data of these samples are summarized in **Table 3.2**. Although the difference in the b^* values is small among the three samples calcined at 1350, 1375, and 1400 ºC, the lowest b^* value was obtained for the sample obtained at 1375 ºC ($b^* = -31.0$). Accordingly, the optimum calcination temperature was 1375 ºC for the synthesis of $(Ca_{0.94}Eu_{0.06})_3Sc_2Si_3O_{12+\delta}$.

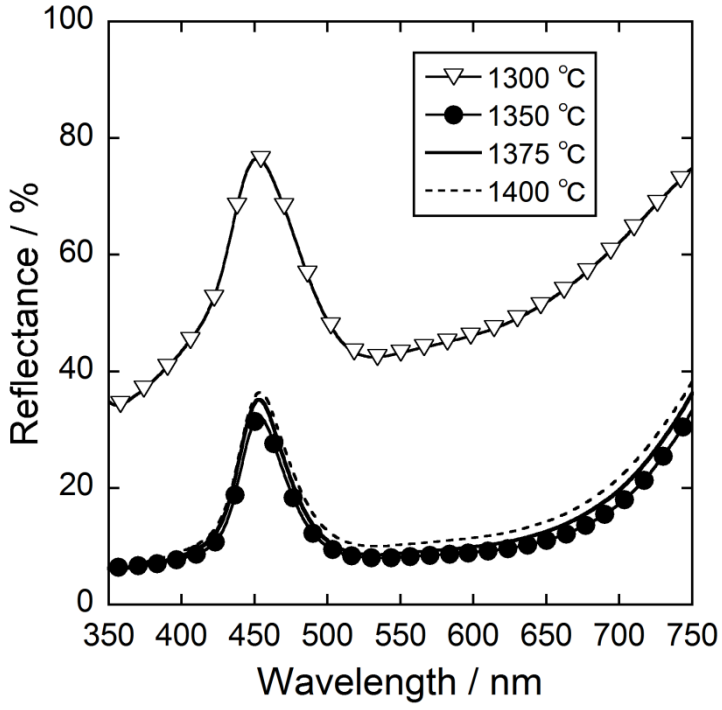

Figure 3.4 UV-Vis diffuse reflectance spectra for the $(Ca_{0.94}Eu_{0.06})_3Sc_2Si_3O_{12+\delta}$ samples calcined at 1300, 1350, 1375, and 1400 ºC for 4 h.

Table 3.2 CIE $L^*a^*b^*$ color coordinate data of the $(Ca_{0.94}Eu_{0.06})_3Sc_2Si_3O_{12+\delta}$ samples calcined at 1300, 1350, 1375, and 1400 ºC for 4 h

Calcination temperature / ºC	L^*	a^*	b^*
1300	72.5	+14.7	−19.8
1350	36.8	+22.9	−30.1
1375	38.0	+23.4	−31.0
1400	41.0	+22.4	−30.1

Then, the calcination time was optimized to obtain the most vivid blue color, where the calcination temperature was fixed at 1375 ºC. **Figure 3.5** shows the XRD patterns of the $(Ca_{0.94}Eu_{0.06})_3Sc_2Si_3O_{12+\delta}$ samples calcined at 1375 ºC for 4, 6, and 8 h. In addition to the garnet-type $Ca_3Sc_2Si_3O_{12}$ phase, SiO_2 and Sc_2O_3 impurity phases were also still observed for all samples.

Figure 3.6 illustrates the UV-Vis diffuse reflectance spectra for these samples. The reflection intensity in the blue light (435 − 480 nm) and yellow light (570 − 590 nm) regions depended on the calcination time. The CIE $L^*a^*b^*$ color coordinate data of the $(Ca_{0.94}Eu_{0.06})_3Sc_2Si_3O_{12+\delta}$ samples calcined at 1375 ºC for 4, 6, and 8 h are summarized in **Table 3.3**. The highest blueness was obtained for the pigment calcined at 1375 ºC for 6 h (b^* = −33.8).

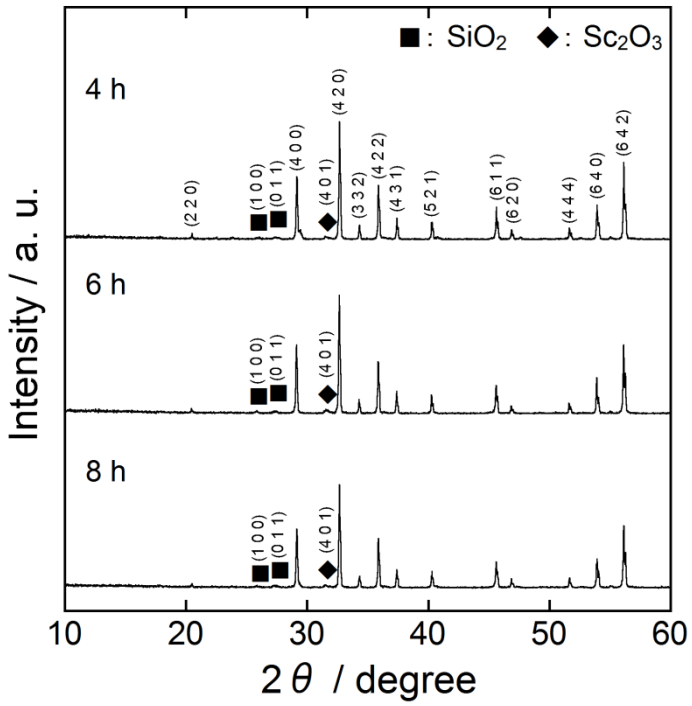

Figure 3.5 XRD patterns of the $(Ca_{0.94}Eu_{0.06})_3Sc_2Si_3O_{12+\delta}$ samples calcined at 1375 ºC for 4, 6, and 8 h.

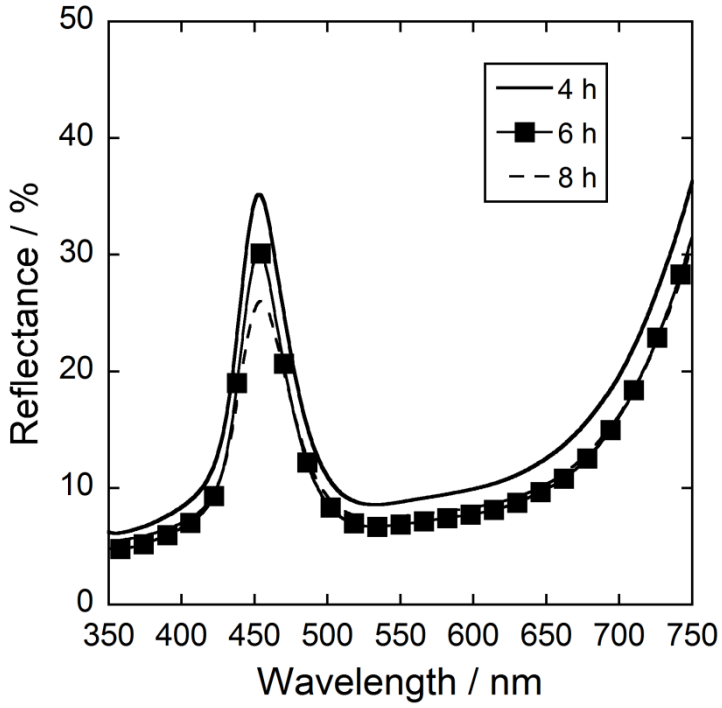

Figure 3.6 UV-Vis diffuse reflectance spectra of the $(Ca_{0.94}Eu_{0.06})_3Sc_2Si_3O_{12+\delta}$ samples calcined at 1375 ºC for 4, 6, and 8 h.

Table 3.3 CIE $L^*a^*b^*$ color coordinate data of the $(Ca_{0.94}Eu_{0.06})_3Sc_2Si_3O_{12+\delta}$ samples calcined at 1375 ºC for 4, 6, and 8 h

Calcination period / h	L^*	a^*	b^*
4	38.0	+23.4	−31.0
6	34.2	+25.6	−33.8
8	34.5	+20.4	−28.2

From the results mentioned above, it was found that the most vivid blue color was obtained for $(Ca_{0.94}Eu_{0.06})_3Sc_2Si_3O_{12+\delta}$ synthesized at 1375 ºC for 6 h. However, the impurity SiO_2 and Sc_2O_3 phases were still observed in addition to the main garnet-type $Ca_3Sc_2Si_3O_{12}$ phase. It is considered that the blue hue of this pigment could be further improved by removing these impurities. For this purpose, the $(Ca_{0.94}Eu_{0.06})_3Sc_2Si_3O_{12+\delta}$ sample synthesized at 1375 ºC for 6 h was washed with a dilute HCl solution (2%). **Figure 3.7** shows the XRD patterns of the $(Ca_{0.94}Eu_{0.06})_3Sc_2Si_3O_{12+\delta}$ samples before and after washing. The integral peak intensities of Sc_2O_3 and $(Ca_{0.94}Eu_{0.06})_3Sc_2Si_3O_{12+\delta}$ were estimated using the diffraction peaks at 2θ = 31.5º and 32.5º for the former and the latter, respectively. The intensity ratio of $I_{Sc_2O_3}/I_{pigment}$ was calculated for each sample, and the results are summarized in **Table 3.4**. The $I_{Sc_2O_3}/I_{pigment}$ slightly decreased after washing, indicating that a small amount of the Sc_2O_3 impurity was removed by the purification process.

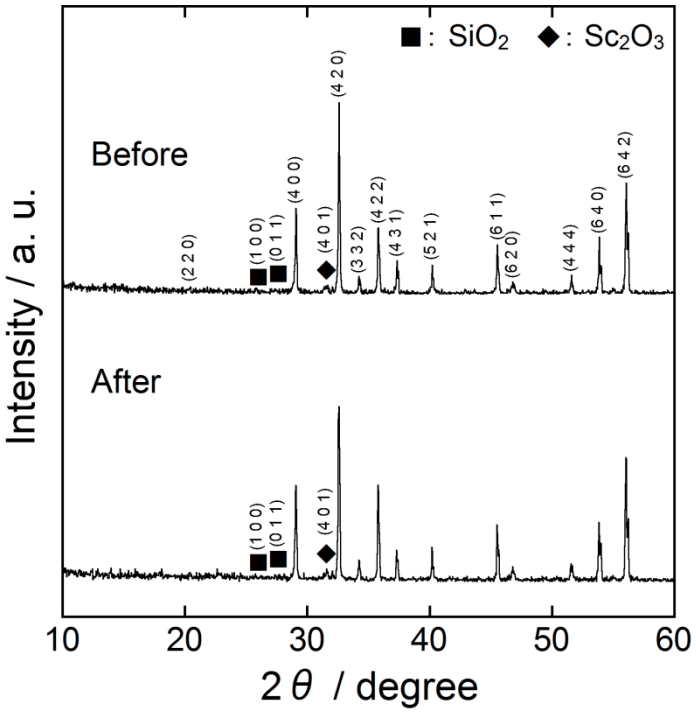

Figure 3.7 XRD patterns of the optimized $(Ca_{0.94}Eu_{0.06})_3Sc_2Si_3O_{12+\delta}$ samples before and after washing with a dilute HCl solution (2%).

Table 3.4 The integral peak intensity ratio of $I_{Sc_2O_3}/I_{pigment}$ before and after washing the $(Ca_{0.94}Eu_{0.06})_3Sc_2Si_3O_{12+\delta}$ pigment with a dilute HCl solution (2%)

Samples	$I_{Sc_2O_3}/I_{pigment}$
$(Ca_{0.94}Eu_{0.06})_3Sc_2Si_3O_{12+\delta}$ (before washing)	0.066
$(Ca_{0.94}Eu_{0.06})_3Sc_2Si_3O_{12+\delta}$ (after washing)	0.042

Figure 3.8 illustrates the UV-Vis diffuse reflectance spectra for the samples before and after washing. The reflection intensity was decreased after washing. The CIE $L^*a^*b^*$ color coordinate data for the samples before and after washing with 2% HCl are summarized in **Table 3.5**, with those for the previous amorphous $(W_{0.76}Eu_{0.24})OP_2O_{7-\delta}$, the commercial

iron hexacyanoferrate (Prussian blue, Dainichiseika Color & Chemicals Mfg., MILORI BLUE 905), and cobalt aluminate blue (Cobalt blue, Dainichiseika Color & Chemicals Mfg., DAIPYROXIDE TM COLOR BLUE#3490E) pigments. The lowest b^* value, −36.3, was obtained for the $(Ca_{0.94}Eu_{0.06})_3Sc_2Si_3O_{12+\delta}$ pigment after washing. Although this blueness value came short of that for the commercial cobalt blue pigment (−64.2), it was significantly larger than those of the commercial iron hexacyanoferrate (−15.6), $(Zr,V)SiO_4$ (−17.6) [9], Al_2O_3-MoO_x (−8.4) [10], $YIn_{0.95}Mn_{0.05}O_3$ (−31.2) [36], and amorphous $(W_{0.76}Eu_{0.24})OP_2O_{7-\delta}$ (−25.2). In addition, the brightness of this pigment (L^* = 31.2) was also higher than that of the commercial iron hexacyanoferrate (L^* = 9.31), and, as a result, the color of the $(Ca_{0.94}Eu_{0.06})_3Sc_2Si_3O_{12+\delta}$ pigment became genuine blue.

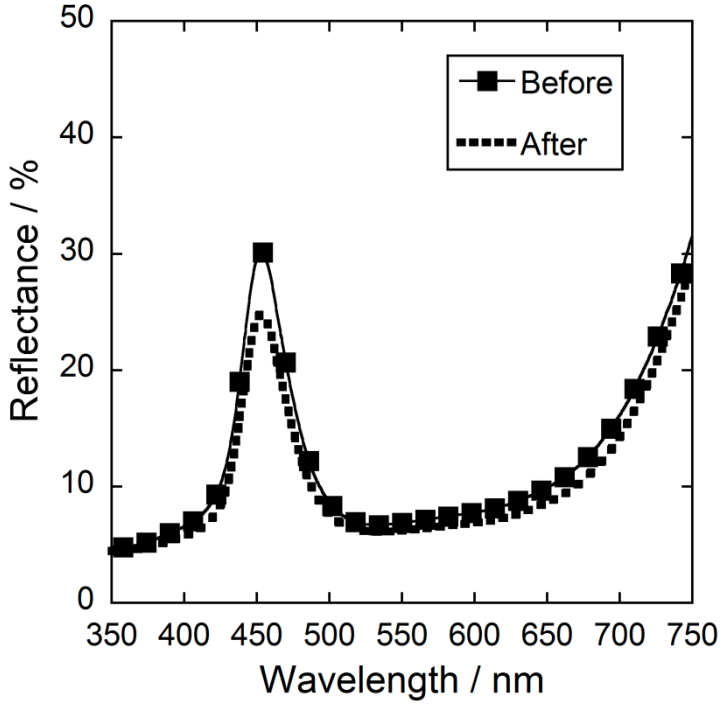

Figure 3.8 UV-Vis diffuse reflectance spectra for the $(Ca_{0.94}Eu_{0.06})_3Sc_2Si_3O_{12+\delta}$ pigments before and after washing with a dilute HCl solution (2%).

Table 3.5 CIE $L^*a^*b^*$ color coordinate data for the pigments

Pigments	L^*	a^*	b^*
$(Ca_{0.94}Eu_{0.06})_3Sc_2Si_3O_{12+\delta}$ (before washing)	34.2	+25.6	−33.8
$(Ca_{0.94}Eu_{0.06})_3Sc_2Si_3O_{12+\delta}$ (after washing)	31.2	+27.7	−36.3
$(W_{0.76}Eu_{0.24})OP_2O_{7-\delta}$	39.2	+10.6	−25.2
Commercial iron hexacyanoferrate ($Fe(III)_4[Fe(II)(CN)_6]_3$, Prussian blue)	9.31	+12.6	−15.6
Commercial cobalt aluminate ($CoAl_2O_4$, Cobalt blue)	34.6	+32.4	−64.2

3.4 Conclusion

Novel garnet-type $(Ca_{1-x}Eu_x)_3Sc_2Si_3O_{12+\delta}$ ($0 \leq x \leq 0.10$) were synthesized as environmentally friendly inorganic blue pigments. The color of the pigments depended on their composition and the synthesis conditions. The most vivid blue color was obtained for the $(Ca_{0.94}Eu_{0.06})_3Sc_2Si_3O_{12+\delta}$ pigment, which was calcined at 1375 ºC for 6 h and subsequently washed with a dilute HCl solution (2%). The blueness value ($b^* = -36.3$) was more brilliant than that of the commercially available iron hexacyanoferrate pigment ($b^* = -15.6$). The present pigment consists of nontoxic and safe elements (Ca, Eu, Sc, Si, and O), and therefore, it should be an attractive alternative for the conventional inorganic blue one.

Summary

In the work of this thesis, novel and environmentally friendly inorganic pigments exhibiting yellow, red, and blue colors have been successfully synthesized and their color properties were characterized to realize advanced coloring materials with high color performances. The results obtained through this work are summarized as follows:

Chapter 1

Novel yellow pigments, $Bi_{1-x-y-z}Ca_xZn_yLa_zVO_{4-(x+y)/2}$ ($0.04 \leq x \leq 0.12$; $0.01 \leq y \leq 0.05$; $0.01 \leq z \leq 0.10$), were successfully synthesized by the evaporation to dryness method, to further improve the yellowness of a $Bi_{0.90}Ca_{0.08}Zn_{0.02}VO_{3.950}$ pigment (b^* = +91.6), which was previously reported by our research group. The color of these pigments depended on their compositions. Among them, the most vivid yellowness (b^*) was obtained for a $Bi_{0.85}Ca_{0.08}Zn_{0.02}La_{0.05}VO_{3.950}$ pigment, with a b^* value of +93.5, which was significantly higher than that of the commercially available $BiVO_4$ pigment (b^* = +80.3). Furthermore, the yellowness of the present $Bi_{0.85}Ca_{0.08}Zn_{0.02}La_{0.05}VO_{3.950}$ pigment (b^* = +93.5) is the best value compared with those of any other environmentally friendly inorganic yellow pigments that have ever reported.

Chapter 2

Novel red pigments, $(Bi_{1-x-y}Zr_xAl_y)_4V_2O_{11+\delta}$ ($0 \leq x \leq 0.15$; $0 \leq y \leq 0.10$), were successfully synthesized by the conventional solid state reaction method. The color of the pigments depended on the calcination atmosphere and the concentrations of Zr^{4+} and Al^{3+}. Among them, the deepest red color was obtained for a $(Bi_{0.92}Zr_{0.07}Al_{0.01})_4V_2O_{11+\delta_{2a}}$ pigment

calcined in a flow of O_2. The redness of this pigment (a^* = +41.9) was significantly higher than that of the commercial Fe_2O_3 pigment (a^* = +28.9).

Chapter 3

Novel blue pigments, $(Ca_{1-x}Eu_x)_3Sc_2Si_3O_{12+\delta}$ ($0 \leq x \leq 0.10$) with the garnet-type structure, were successfully synthesized by the conventional solid state reaction method. A bright-blue color was realized by doping divalent Eu^{2+} ions into the Ca^{2+} sites in the $Ca_3Sc_2Si_3O_{12}$ lattice, and the color of the pigments was dependent on their compositions and the preparation conditions. The most brilliant blue hue has been achieved for the $(Ca_{0.94}Eu_{0.06})_3Sc_2Si_3O_{12+\delta}$ pigment, which was calcined at 1375 ºC for 6 h in a flow of 2%H_2−98%Ar and subsequently washed with a dilute HCl solution (2%). This pigment exhibited bright blue color as the brightness and blueness values (L^* = 31.2, b^* = −36.3) were obviously higher than those of the commercially available Prussian blue ($Fe(III)_4[Fe(II)(CN)_6]_3$) pigment ($L^*$ = 9.31, b^* = −15.6).

References

[1] *High Performance Pigments*, ed. by E.B. Faulkner, R.J. Schwartz, Wiley-VCH, Weinheim, 2009. doi: 10.1002/9783527626915.

[2] *Industrial Inorganic Pigments*, ed. by G. Buxbaum, G. Pfaff, Wiley-VCH, Weinheim, 2005. doi:10.1002/3527603735.

[3] P. Maestro, D. Huguenin, *J. Alloys Comp.*, 1995, **225**, 520−528.

[4] G. Gauthier, S. Jobic, M. Evain, H.-J. Koo, M.-H. Whangbo, C. Fouassier, R. Brec, *Chem. Mater.*, 2003, **15**, 828−837.

[5] M. Jansen, H.P. Letschert, *Nature*, 2000, **404**, 980−982.

[6] N. Diot, O. Larcher, R. Marchand, J.Y. Kempf, P. Macaudière, *J. Alloys Comp.*, 2001, **323−324**, 45−48.

[7] R.A. Candeia, M.I.B. Bernardi, E. Longo, I.M.G. Santos, A.G. Souza, *Mater*. *Lett*., 2004, **58**, 569−572.

[8] G. George, G. George, P.P. Rao, M.L. Reddy, *Chem*. *Lett*., 2005, **34**, 1702–1703.

[9] L.M. Schabbach, F. Bondioli, A.M. Ferrari, T. Manfredini, C.O. Petter, M.C. Fredel, *J. Eur*. *Ceram*. *Soc*., 2007, **27**, 179−184.

[10] M. Dondi, F. Matteucci, G. Baldi, A. Barzanti, G. Cruciani, I. Zama, C.L. Bianchi, *Dyes Pigm*., 2008, **76**, 179−186.

[11] G. George, L.S. Kumari, V.S. Vishnu, S. Ananthakumar, M.L.P. Reddy, *J. Solid State Chem*., 2008, **181**, 487–492.

[12] S.K. Biswas, D. Dhak, A. Pathak, P. Pramanik, *Mater*. *Res*. *Bull*., 2008, **43**, 665–675.

[13] N. Pailhé, M. Gaudon, A. Demourgues, *Mater*. *Res*. *Bull*., 2009, **44**, 1771–1777.

[14] V.S. Vishnu, G. George, V. Divya, M.L.P. Reddy, *Dyes Pigm*., 2009, **82**, 53–57.

[15] V.S. Vishnu, M.L. Reddy, *Chem*. *Lett*., 2010, **39**, 820–821.

[16] V.S. Vishnu, G. George, M.L.P. Reddy, *Dyes Pigm*., 2010, **85**, 117–123.

[17] L.S. Kumari, P.P. Rao, P. Koshy, *J. Am. Ceram. Soc*., 2010, **93[5]**, 1402−1408.

[18] P. Šulcová, L. Vitásková, M. Trojan, *J. Therm. Anal. Calorim*., 2010, **99**, 409−413.

[19] M. Llusar, L. Vitásková, P. Šulcová, M.A. Tena, J.A. Badenes, G. Monrós, *J. Eur. Ceram. Soc*., 2010, **30**, 37−52.

[20] L.S. Kumari, T.H. Gayathri, S.F. Sameera, P.P. Rao, *J. Am. Ceram. Soc*., 2011, **94[2]**, 320−323.

[21] P. Šulcová, P. Bystrzycki, L. Válek, M. Trojan, *J. Min. Metall. Sect. B-Metall*., 2011, **47(2)B**, 105–112.

[22] V.S. Vishnu, S. Jose, M.L. Reddy, *J. Am. Ceram. Soc*., 2011, **94[4]**, 997–1001.

[23] V.S. Vishnu, M.L. Reddy, *Sol. Energy Mater. Sol. Cells*, 2011, **95**, 2685–2692.

[24] G. George, V.S. Vishnu, M.L.P. Reddy, *Dyes Pigm*., 2011, **88**, 109–115.

[25] P. Šulcová, J. Večeřa, P. Bystrzycki, *J. Therm. Anal. Calorim*., 2012, **108**, 525−529.

[26] L. Stránská, P. Šulcová, J. Mouchová, *J. Therm. Anal. Calorim*., 2012, **109**, 643−648.

[27] P. Luňáková, M. Trojan, J. Luxová, J. Trojan, *Dyes Pigm*., 2013, **96**, 264–268.

[28] T. Masui, H. Tategaki, N. Imanaka, *J. Mater. Sci*., 2004, **39**, 4909−4911.

[29] T. Masui, S. Furukawa, N. Imanaka, *Chem. Lett*., 2005, **34**, 1322−1323.

[30] T. Masui, S. Furukawa, N. Imanaka, *Chem. Lett*., 2006, **35**, 1032−1033.

[31] S. Furukawa, T. Masui, N. Imanaka, *J. Alloys Comp*., 2008, **451**, 640−643.

[32] N. Imanaka, T. Masui, S. Furukawa, *Chem. Lett*., 2008, **37**, 104−105.

[33] T. Masui, A. Shiraishi, S. Furukawa, Wendusu, N. Nunotani, N. Imanaka, *J. Jpn. Soc. Colour Mater*., 2012, **85[1]**, 9−13.

[34] Wendusu, D. Kato, T. Masui, N. Imanaka, *Bull. Chem. Soc. Jpn*., 2013, **86**, 283−288.

[35] A.E. Smith, H. Mizoguchi, K. Delaney, N.A. Spaldin, A.W. Sleight, M.A. Subramanian, *J. Am. Chem. Soc*., 2009, **131**, 17084−17086.

[36] M. Ocaña, J.P. Espinós, J.B. Carda, *Dyes Pigm*., 2011, **91**, 501–507.

[37] H.-H. Liu, C.-Y. Chen, G.-I. Chen, L.-H. Lee, H.-L. Chen, *Int. Arch. Occup. Environ. Health*, 2012, **85**, 447–453.

[38] A. Walsh, Y. Yan, M.N. Huda, M.M. Al-Jassim, S.-H. Wei, *Chem*. *Mater*., 2009, **21**, 547–551.

[39] S. Tokunaga, H. Kato, A. Kudo, *Chem*. *Mater*., 2001, **13**, 4624–4628.

[40] A. Kudo, K. Omori, H. Kato, *J*. *Am*. *Chem*. *Soc*., 1999, **121**, 11459−11467.

[41] M. Oshikiri, M. Boero, J. Ye, Z. Zou, G. Kido, *J*. *Chem*. *Phys*., 2002, **117**, 7313–7318.

[42] J. Yu, A. Kudo, *Adv*. *Funct*. *Mater*., 2006, **16**, 2163–2169.

[43] D. Ke, T. Peng, L. Ma, P. Cai, K. Dai, *Inorg*. *Chem*., 2009, **48**, 4685–4691.

[44] R.D. Shannon, *Acta Crystallogr*. *Sect*. *A*, 1976, **32**, 751–767.

[45] G.K. Williamson, W.H. Hall, *Acta Metall*., 1953, **1**, 22−31.

[46] D.R. Eppler, R.A. Eppler, *Ceram*. *Eng*. *Sci*. *Proc*., 1996, **17**, 77–87.

[47] M. Kato, M. Takahashi, *J*. *Mater*. *Sci*. *Lett*., 2001, **20**, 413–414.

[48] R.L. Frost, D.A. Henry, M.L. Weier, W. Martens, *J*. *Raman Spectrosc*., 2006, **37**, 722–732.

[49] K.A. Winship, *Adverse Drug React*. *Acute Poisoning Rev*., 1983, **2**, 103−121.

[50] S.J. Patwe, A. Patra, R. Dey, A. Roy, R.M. Kadam, S.N. Achary, A.K. Tyagi, *J*. *Am*. *Ceram*. *Soc*., 2013, **96 [11]**, 3448−3456.

[51] K. Sooryanarayana, T.N. Guru Row, K.B.R. Varma, *Mater. Res. Bull*., 1997, **32**, 1651−1656.

[52] I. Abrahams, F. Krok, *J*. *Mater*. *Chem*., 2002, **12**, 3351−3362.

[53] A.W. Sleight, H.-y. Chen, A. Ferretti, D.E. Cox, *Mater*. *Res*. *Bull*., 1979, **14**, 1571−1581.

[54] S. Poulston, N.J. Price, C. Weeks, M.D. Allen, P. Parlett, M. Steinberg, M. Bowker, *J*.

Catal., 1998, **178**, 658−667.

[55] H. Fan, G. Wang, L. Hu, *Solid State Sci*., 2009, **11**, 2065−2070.

[56] J. Sun, X. Li, Q. Zhao, J. Ke, D. Zhang, *J. Phys. Chem. C*, 2014, **118**, 10113−10121.

[57] A. Demourgues, C. Dussarrat, R. Bontchev, B. Darriet, F. Weill, J. Darriet, *Nucl. Inst. Meth. Phys. Res.*, 1995, **97**, 82−88.

[58] Z.S. Teweldemedhin, K.V. Ramanujachary, M. Greenblatt, *Mater. Res. Bull*., 1993, **28**, 427−434.

Acknowledgements

The author would like to express his heartfelt gratitude to Professor Dr. Nobuhito Imanaka, Department of Applied Chemistry, Graduate School of Engineering, Osaka University, for his continuous guidance, many invaluable suggestions, and his science encouragement throughout the work. The author is indebted to Dr. Toshiyuki Masui, Department of Applied Chemistry, Graduate School of Engineering, Osaka University, for his continuous guidance and stimulating discussions for carrying out this work. The author is also very grateful to Dr. Shinji Tamura, Department of Applied Chemistry, Graduate School of Engineering, Osaka University, for his helpful suggestions and apposite advice.

The author is obliged to Dr. Hirokazu Izumi, Hyogo Prefectural Institute of Technology, for XPS measurements. Furthermore, the author desires to express his sincere thanks to Dr. Toshihiro Okajima, Dr. Hiroyuki Setoyama, and Dr. Daiki Murakami in Kyushu Synchrotron Light Research Center (SAGA Light Source), for their assistance with the XANES measurement. In addition, the author is grateful to Mr. Atsunori Shiraishi in Saga Ceramics Research Laboratory, for his assistance with the XANES measurement and his helpful suggestions and heartfelt advice.

The author is deeply grateful to Professor Dr. Susumu Kuwabata, Department of Applied Chemistry, Graduate School of Engineering, Osaka University, and Professor Dr. Ken-ichi Machida, Department of Applied Chemistry, Graduate School of Engineering, Osaka University, for reviewing this thesis and giving their valuable comments.

Special thanks should be given to author's seniors and co-workers, Dr. Keisuke Yasuda, Dr. Sun Woog Kim, Dr. Naoyoshi Nunotani, Dr. Soichiro Tsujimoto, Mr. Shinya Furukawa, Mr. Daisuke Kato, Mr. Ken-ichi Ikawa, Mr. Taihei Honda, Ms. Ayaka Hosoya, Mr.

Hiroki Nakado, Mr. Yoshinori Fukusumi, Mr. Naoki Takeuchi, and Mr. Tetsuro Yoshida, for their helpful assistance and support in the course of this work, and the other members of the research group under direction of Professor Dr. Nobuhito Imanaka, Osaka University.

The Japan Society for the Promotion of Science is also acknowledged for a research fellowship.

Finally, the author would like to extend deep gratitude to his parents, Mr. Batuhexige and Mrs. Narentuya, his younger sister, Ms. Surina, and all members of his family for their encouragement, continuous understanding, and perpetual supports.